A Fast Numerical Method for the Interfacial Motion of a Surfactant-Laden Bubble in Creeping Flow

by

Enkeleida Lushi

B. Sc. Hon., Simon Fraser University, 2004

A THESIS SUBMITTED IN PARTIAL FULFILLMENT
OF THE REQUIREMENTS FOR THE DEGREE OF
MASTER OF SCIENCE
IN THE DEPARTMENT
OF
MATHEMATICS

SIMON FRASER UNIVERSITY
Summer, 2006

APPROVAL

Name: Enkeleida Lushi

Degree: Master of Science

Title of thesis: A Fast Numerical Method for the Interfacial Motion of a Surfactant-Laden Bubble in Creeping Flow

Examining Committee: Dr. Rustum Choksi
Chair

Dr. Mary Catherine A. Kropinski
Senior Supervisor

Dr. Robert D. Russell
Supervisor

Dr. John M. Stockie
Supervisor

Dr. Ralf W. Wittenberg
Internal Examiner

Date Approved: July 12, 2006

Abstract

Numerical simulation is an important contemporary tool used to investigate interfacial motion in complex fluids. Even with increasing computer speed and memory, fast, efficient and highly accurate algorithms that are able to handle large-scale long-time simulations, are needed.

We present a new robust numerical method for computing the motion of a two-dimensional bubble interface in a straining Stokes Flow laden with surfactants, which induce nonuniform surface tension. This consists of evolving a convective-diffusive equation describing the surfactant dynamics, coupled with the interface motion equations. The interface velocity is found by solving an integral equation derived from the complex variable theory of the biharmonic equation. The numerical method solving the integral equations is spectrally accurate and employs a Fast Multipole-based iterative method. We investigate an Implicit-Explicit time-stepping method to ease the stability constraint. By maintaining an equal arclength point spacing, we maximize the time-stepping scheme's efficiency.

Acknowledgments

I am most grateful to Dr. Mary Catherine Kropinski, an invaluable mentor and role model throughout my undergraduate and graduate degrees, for introducing me to interesting mathematical and computational problems, and for providing generous funding for this research.

Many thanks go to my colleague Jeffrey Gilmore, for helping me understand many mathematical and numerical concepts used in this project.

I also like to thank the Applied Mathematics faculty, in particular Dr. Robert Russell and Dr. John Stockie, for their helpful advice on research projects and career choices.

Finally, I would like to express my deepest gratitude to my family, fiancee and friends who have accompanied and constantly supported me in coming so far.

Contents

Abstract iii
Acknowledgments iv
Contents v
List of Tables vii
List of Figures viii
1 Introduction 1
1.1 Surfactants and their Importance 2
1.2 Background on the Mathematical Work 3
1.3 Overview of the Thesis 4
2 The Mathematical Model 6
2.1 Governing Equations for the Bubble Interface 6
2.2 The Surfactant Partial Differential Equation 11
2.3 The Biharmonic Equation Theory 13
2.4 The Sherman-Lauricella Integral Equations 17
3 The Equal Arclength Frame 19
3.1 The Interface Motion 20
3.2 Modification of the Surfactant Equation 21
3.3 The Parametrization of the Integral Equations 23
3.4 The System of Time Evolution Equations 25
4 The Numerical Implementation 26
4.1 Spectral Description of the Functions 26
4.2 Discretization of the Integral Equations 28
4.3 Time Integration Methods for the Interface 30
4.4 Time Integration Methods for the Surfactant 32

5 Accuracy, Stability, Convergence 34
5.1 Comparisons to Analytical Solutions 34
5.2 The Order of Temporal Convergence 40
5.3 The Numerical Stability of the Schemes 42
6 Various Numerical Investigations 47
6.1 Surfactant Caps on Bubbles 47
6.2 Comparisons for Diminishing Surfactant Influence 48
6.3 Surfactant and Bubble Breakup 49
6.4 Bubbles and Non-Uniform Surfactant 49
7 Conclusion and Future Work 54
7.1 Future Work 55
Bibliography 56

List of Tables

5.1 Comparison with the analytical solution: the errors at time T=0,4,8,...,32. . 39
5.2 Comparison with the analytical solution: the errors for different Δt. 39

6.1 Comparisons of diminishing surfactant effects on the bubble interface at T=2. 48
6.2 Comparisons of diminishing surfactant effects on the bubble interface at T=7. 48

List of Figures

1.1 Strain flow and the surfactant layer on the bubble 2

2.1 A bubble in an infinite viscous fluid expanse and the domain geometry. . . . 8

5.1 Comparison with the analytical solution: the bubble profile 37
5.2 Comparison with the analytical solution: the surfactant profile 38
5.3 The errors in the bubble area and surfactant total for four different time-steps. 41
5.4 The numerical accuracy in the calculation of the bubble area, total amount of surfactant, interface position and surfactant concentration. 41
5.5 The Fourier transforms $\log(\hat{zeta}_k)$ of the evolution of an initially circular bubble with parameters $Q = 0.51$, $Pe_s = 10^3$, $\beta = 0.1$ at times 0:0.5:1 in an unpadded and padded computation. 43
5.6 The instantaneous eigenvalues of the Jacobian Matrix for the interface ζ. . . 44
5.7 The instantaneous eigenvalues of the Jacobian Matrix for the surfactant Γ. . 45
5.8 The instantaneous eigenvalues of the Jacobian Matrix for the surfactant Γ: local plot. 46

6.1 Surfactant cap occurrences for $\beta = 0.1$, $Pe_s = 10^3$. 50
6.2 Superimposed plots of the interface, surfactant and surface tension profiles at $T = 7$ for diminishing β 51
6.3 Bursting bubble profiles at time $T = 7$ for parameters $Q = 0.40$, $Pe_s = 10$ and different surfactant influence $\beta = 0.0, 0.1$ and 0.2. 52
6.4 Bubble bursting, the surfactant profiles for $\beta = 0.2$ and $\beta = 0.1$. 53
6.5 Effects of non-uniform initial surfactant profiles on initially circular bubbles. . 53

Chapter 1

Introduction

Although their manifestation often goes unnoticed, bubbles play such a significant role in so many aspects of everyday events that it would not be an exercise in hyperbole to describe them as omnipresent. The ubiquity and importance of bubbles is clear as enhancers in sparkling beverages, in fermentation of food or in cooking processes. Their role however extends beyond the culinary aspects, and their understanding is paramount in as diverse fields as hydrocarbon seepage in ocean floors, aerosol chemical manufacturing, wave breaking, bacteria transport, photosynthesis and even pulmonary functions.

The study of bubbles has thus fascinated physicists and mathematicians for a long time and their evolution has been studied extensively. Some of the pioneering work in the study of bubble deformation in extensional, shear or straining, viscous flow was done by G.I. Taylor [23]. Some of his well-known hydrodynamics experiments feature a bubble or drop in the midst of four rotating cylinders that produce a straining-type flow, as shown in the Figure 1.1. The shear flow induced the bubble to stretch, and the resulting shapes were steady or unsteady depending on the strain parameters. The existence of steady or unsteady (bursting) bubbles observed in these experiments was confirmed in later studies [6]. Other phenomena were reported from the various experiments performed in the area, such as tip streaming, cusped bubble or other bubble deformation modes for different flow parameters [8]. It is believed that the non-uniform concentration of *surfactant*, or surface active agent, on the bubble surface affects these deformations and facilitates the bubble breakup or fracture if the strain in the flow is significant. For example, surfactant accumulates at the bubble tips in the Taylor straining-type flow in Fig. 1.1, and these surfactant caps are believed to be the culprit for different terminal bubble shapes obtained, e.g cusped/sigmoidal bubbles.

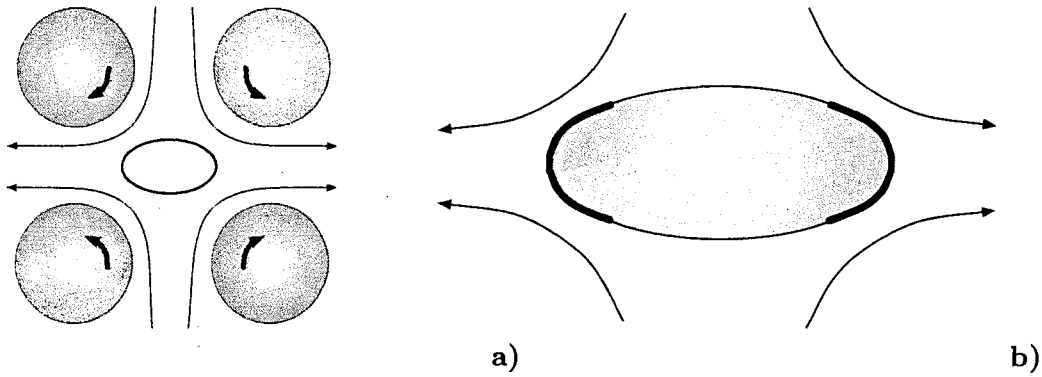

Figure 1.1: *Strain flow and the non-uniform surfactant layer on the bubble: a) Taylor's strain-type flow driven by four rollers and the bubble in the midst. b) Surfactant is advected by the flow towards the bubble tips where it accumulates and eventually forms stagnant caps.*

1.1 Surfactants and their Importance

What are surfactants and how do they figure out in practice? Surfactants, or *sur*face *act*ive *agents*, are substances that have molecules with a hydrophobic and hydrophilic part. The hydrophobic part aligns itself to air, while the hydrophilic part aligns itself to water; thus surfactants tend to be found at interfaces. Dish-washing soap is a familiar surfactant, but many substances, including salt and fatty acids, can act as surfactants. They are active in detergents, emulsifiers, paints, adhesives, inks, alveoli, and play a critical role in numerous industrial and biomedical applications ranging from enhanced oil recovery to pulmonary functions. An important effect of surfactants is that they alter the surface tension, which alters the interface hydrodynamics; thus there exists ample interest in understanding them.

Surfactants are convected and diffused along interfaces by the motion of the fluid and by molecular diffusion respectively. The surface tension depends on the surfactant distribution through an *equation of state*; regions of higher surfactant concentration have lower surface tension. Nonuniform surfactant concentration along an interface creates nonuniform normal and tangential forces in the fluid. This affects the fluid velocity, which in turn affects the surfactant distribution. For example, the convection of surfactant toward the stagnation points at the bubble's tip lowers the surface tension there and increases the bubble deformation. On the other hand, the tangential forces resist the convection of surfactant toward the bubble tip and so restrain the deformation of the bubble. Dilation/compression of the interface also results in a corresponding decrease/increase in the surfactant concentration.

1.2 Background on the Mathematical Work

It would be preferable to have mathematical solutions for a three-dimensional bubble interface problem for better understanding of the phenomena observed experimentally; however, these are difficult to obtain either analytically and computationally. The interface of the bubble is evolving together with the flow in the domains it separates, and this makes the problem intricate. Numerically computing the motion of interfaces with surfactant is even more challenging. The Navier-Stokes equations must be solved in a complex moving domain with prescribed jumps in the normal and the tangential stress across the interface separating the domains. The moving interface must be accurately simulated and topological transitions may occur as interfaces become ramified and break-up. Further, as surfactant is advected and diffused along the interface, there may be adsorption/desorption of surfactant from/to the bulk to/from the interface and this must be accurately accounted for.

Significant work has been done on simplified models of two-dimensional drops and bubbles. In most cases these two-dimensional models are found to behave similarly to the corresponding three-dimensional bubbles observed in experiments [2]. Tanveer and Vasconcelos [22] obtained some analytical solutions for the bubble interfaces with no surfactant by using the theory of the biharmonic equation into which the Stokes Equations in two-dimensional flows reduces. However, the solutions they present are for a certain class of polynomial initial bubble shapes, which restricts the scope of the investigations as the bubbles have certain symmetry. In particular, general bubble shapes and multiple bubble interactions cannot be studied by this approach.

Kropinski [13, 14] overcomes both of these aforementioned limitations by numerically computing the evolution of bubble and drop interfaces in a clean, or no surfactant, flow. These computations use an accurate and efficient integral equation formulation of the problem developed by Greengard, et al [10]. The discretization of the integral equation is spectrally accurate and the matrix-vector products are computed using the Fast Multipole Method [7]. Another notable feature of these computations is the use of ideas presented in [11] to remove the numerical stiffness from the evolution of the interface. By dynamically maintaining a mesh in which the marker points are equi-distributed, the time intervals are only linearly dependent on the space intervals. This implementation allowed long-time bubble simulations [13], as well as multiple particle computations [14].

The computations in the above implementation are however limited in cases when the surface tension is constant, because surfactant is not involved. In the case where a bubble is coated with surfactant, the surface tension varies, and thus it alters the interface motion. Analytical solutions for surfactant-laden interfaces have been considered by Siegel [20, 21] and Gilmore [9], which use the afore-noted complex variable theory for a polynomial class of bubbles and investigate their steady-state or time-dependent surfactant concentration profiles. Numerical solutions to the time-dependent problem were also obtained among others by Milliken and Leal [16], Johnson and Borhan [12] and Pozrikidis [18], with the later employing an implicit finite-volume numerical method to the boundary-integral formulation of the problem. These approaches shed insight into the problem, but are not suited for simulating long-time, large-scale multiple interface interactions.

There was the need thus to develop efficient, robust, and highly accurate numerical methods for the varying surface tension case, of the kind developed for the no-surfactant flows in [13, 14], that can handle large-scale, long-time simulations. This motivated the incorporation of the surfactant concentration dynamics into the numerical model for the bubble interfaces in extensional flows. This algorithm would be most beneficial for large-scale problems consisting of a number of interfaces; however in this project we will only develop and analyze the single bubble interface problem, while laying the groundwork for the ideas to be used in further studies.

1.3 Overview of the Thesis

The focus of this project is to develop a new method that efficiently computes numerical solutions for the variable surface tension, or surfactant-laden, single bubble interface in a highly viscous strain flow. Incorporating surfactant dynamics into the problem involves an additional term in the stress balance boundary condition on the interface [20], and solving a convective-diffusive partial differential equation for the evolution of surfactant concentration [24]. For simplicity, in this project we focus on the case of insoluble surfactant where the surfactant remains bound to the interface and its flux into the flow is zero; however, the model can be modified to account for a non-zero surfactant flux. We will elaborate on the case of a single bubble interface in pure strain flow, though the model can be adapted for a variety of extensional flows, as well as heavier malleable particulates (drops).

In Chapter 2 of this thesis, we summarize the mathematical model of time-evolving bubbles with surfactant in a slow viscous flow. First, the governing Stokes' Flow equations are derived from the more general Navier-Stokes equations. The boundary conditions particular to the variable surface tension, hence surfactant, case are defined and the partial differential equation for the surfactant concentration evolution is explained. The complex variable theory for the biharmonic equation is employed to derive the boundary integral equations that describe the interface velocity and thus bubble interface evolution, in a linear strain flow.

In Chapter 3, we look at a new formulation of the problem that enables equal spacing for the marker points describing the bubble interface. This approach aims to side-track numerical stiffness, since the Lagrangian description of the interface is prone to point clustering in high-curvature regions and makes long-time numerical computations expensive. We next modify the partial differential equation for the surfactant concentration to fit this new formulation, as well as explain the parametrization of the integral equations.

In Chapter 4 we examine in some detail the numerical implementation of the problem, how the equations are discretized and explain their suitability and efficiency. We investigate the integration methods chosen for the interface and the surfactant evolutions. The nature of the equations requires specific numerical methods to be used for the interface and the surfactant, and we explain the reasons behind the choices.

In Chapter 5, we look at the accuracy, stability and convergence of the algorithm and check that the model behaves as expected. The analytical solutions of Siegel [20, 21] and Gilmore [9] are used as test cases to validate our model. Next, we check the accuracy of the numerical methods. The numerical stability of the algorithm is discussed last, as well as the high wave-number instabilities encountered and ways to alleviate them.

In Chapter 6 we look at some examples to show the versatility of the numerical model in investigating some interesting physical problems. One inquiry is the formation of surfactant caps as the strain gets larger. We note some differences between surfactant-laden and clean flows. Another investigation is the role that surfactants play on bubble instability, or bursting. To show some advantages of the new model, we present as well time-evolutions of bubbles with non-uniform initial surfactant layers.

In the last chapter we present a summary of our results and draw some conclusions on the work. We outline as well some problems to be tackled in future research.

Chapter 2

The Mathematical Model

In this chapter, we present the equations and boundary conditions in the mathematical model for the surfactant-laden bubble interface considered in our study. We follow closely the models presented in [22, 13, 14] for the constant surface tension case and [20, 21] for the variable surface tension problem case. In the first section we describe the equations governing the slow viscous flow. In the second section we present the equation governing the surfactant distribution. Next, we elaborate on the problem reformulation in the complex-variable theory of the biharmonic equation and the suitable boundary integral representations.

2.1 Governing Equations for the Bubble Interface

The equations for slow viscous flow are a special case of the Navier-Stokes equations. If we assume the flow is incompressible, we have

$$\mathbf{u}_t + (\mathbf{u} \cdot \nabla)\mathbf{u} = -\frac{1}{\rho}\nabla p + \nu \nabla^2 \mathbf{u}, \tag{2.1}$$

$$\nabla \cdot \mathbf{u} = 0, \tag{2.2}$$

where $\mathbf{u}$ is the velocity, p is the pressure, ρ is density, μ is viscosity, and $\nu = \mu/\rho$ is the kinematic viscosity. Suppose that U and L are characteristic values of velocity and length. Equation (2.1) can be non-dimensionalized with the following substitutions:

$$\mathbf{u} = U\bar{\mathbf{u}}, \quad \mathbf{x} = L\bar{\mathbf{x}}, \quad p = \frac{U\mu}{L}\bar{p}, \quad t = \frac{L}{U}\bar{t}. \tag{2.3}$$

(2.1) now appears as

$$R[\bar{\mathbf{u}}_{\bar{t}} + (\bar{\mathbf{u}} \cdot \nabla)\bar{\mathbf{u}}] = -\nabla\bar{p} + \nabla^2\bar{\mathbf{u}},$$

where

$$R = \frac{UL}{\nu}$$

is the Reynolds number, and spatial derivatives are taken to be non-dimensional. R is the ratio of inertial forces to viscous forces and the value of this number characterizes the nature of the flow. When R is small ($R \ll 1$), the inertial terms become negligible and the viscous and pressure terms dominate the flow. Low Reynolds number flow is also known as slow viscous flow, or creeping flow, and is described by the Stokes Equations, which in non-dimensional form are

$$\nabla p = \nabla^2\mathbf{u} \tag{2.4}$$

$$\nabla \cdot \mathbf{u} = 0. \tag{2.5}$$

With the governing equations of slow viscous flow, we now consider the problem of an infinite cylindrical bubble placed in a two-dimensional flow of this type. Motion in the fluid will interact with the fluid/bubble interface causing it to deform.

From now on, general vector notation is taken to be two-dimensional, i.e. $\mathbf{x} = (x, y, 0)$ and $\mathbf{u}(x, y) = (u, v, 0)$. We assume that we are dealing only with bubbles; i.e. the interface encloses a gas with negligible viscosity. The fluid domain is therefore exterior to the bubble. The case of a drop deformation, in which the interface is a barrier between two viscous fluids, is outside the scope of this thesis.

Figure 2.1 illustrates the two-dimensional fluid domain and the bubble interface C. The unit normal $\mathbf{n}$ points out of the fluid domain, or into the bubble interior, and the unit tangent $\mathbf{s}$ is in the clockwise direction. The angle tangent to the bubble interface C is called θ and the local curvature is given by $\kappa = \theta_s$.

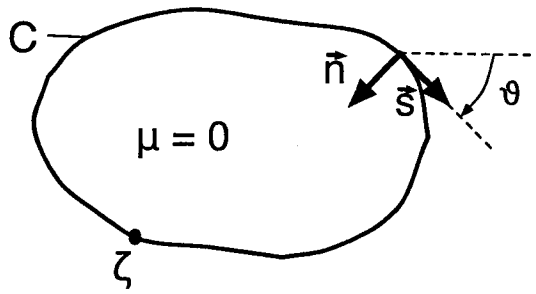

Figure 2.1: *A bubble in an infinite viscous fluid expanse and the domain geometry. The interface is denoted by C, the unit normal* $\mathbf{n}$ *points in the interior and the unit tangent* $\mathbf{s}$ *is in the clockwise direction. The tangent angle to C is denoted by* θ *and the local curvature is given by* $\kappa = \theta_s$

The boundary conditions for this problem are given on the bubble interface C and in the far-field, as $|\mathbf{x}|$ approaches infinity.

We consider the far-field conditions first. We assume that far from the bubble the velocity of the incident flow is linear. The velocity far-field condition appears as

$$\mathbf{u} \sim \mathbf{u}_\infty + \mathcal{O}(1/|\mathbf{x}|^2) \quad \text{for} \quad |\mathbf{x}| \to \infty, \tag{2.6}$$

where

$$\mathbf{u}_\infty = \tfrac{1}{2} \begin{pmatrix} \alpha_0 & \beta_0 - \omega_0 \\ \beta_0 + \omega_0 & -\alpha_0 \end{pmatrix} \cdot \mathbf{x}. \tag{2.7}$$

Here ω_0 is the vorticity of the far-field flow, while α_0 and β_0 characterize its strain rate. For a pure strain flow, we have $\beta_0 = 0, \omega_0 = 0$ and hence $\mathbf{u}_\infty = \frac{1}{2}(\alpha_0 x, -\alpha_0 y)$. On the other hand, the pressure far-field condition is

$$p \sim p_\infty \quad \text{for} \quad |\mathbf{x}| \to \infty, \tag{2.8}$$

where the far-field pressure term p_∞, is a constant determined as part of the solution.

The bubble surface evolves in time making this a moving or *free boundary value problem.* On the bubble surface we must ensure a balance of stresses, which is written as:

$$-p\mathbf{n} + 2\mu\mathbf{E}\mathbf{n} = \sigma\kappa\mathbf{n} + \nabla_s\sigma \tag{2.9}$$

where $\mathbf{E}$ is the rate of strain tensor whose j, k component is given by

$$e_{j,k} = \frac{1}{2}\left(\frac{\partial u_j}{\partial x_k} + \frac{\partial u_k}{\partial x_j}\right).$$

Indices j and k can take on the values 1 or 2 corresponding to the x or y-directions. Here, $\nabla_s = (\mathbf{I}-\mathbf{nn^t})\cdot\nabla$ is the surface gradient, which in two dimensions is a derivative with respect to arclength $\nabla_s = \mathbf{s}\frac{\partial}{\partial s}$. The curvature is denoted by κ, while σ represents the non-uniform surface tension and is non-dimensionalized by σ_0, which is chosen to be a characteristic value for the surface tension, usually that used in the clean flow case. It is through σ that the surfactant concentration influences the interface motion. Note that the model presented here does not account for a surfactant flux of surfactant to/from the exterior fluid domain.

We can determine the velocity $\mathbf{u}$ in the exterior domain, particularly on the bubble interface, from the Stokes Equations. But this is a steady-state solution; how is the time-evolution of the bubble interface determined? This is done by using the kinematic boundary condition, which says that material point $\mathbf{x}$ on the interface advances according to the normal fluid velocity at that point, or

$$\frac{\mathrm{d}\mathbf{x}}{\mathrm{d}t} = (\mathbf{u}\cdot\mathbf{n})\mathbf{n}. \tag{2.10}$$

We complete the problem description by presenting the non-dimensionalization of the boundary conditions. We now choose the characteristic value U to be

$$U = \frac{\sigma_0}{\mu}.$$

This choice conveniently removes characteristic values from the stress interface condition which after dropping the bars becomes:

$$\begin{aligned} -\frac{\sigma_0}{L}\bar{p}\mathbf{n} + 2\frac{\sigma_0\mu}{L}\overline{\mathbf{E}}\cdot\mathbf{n} &= \frac{\sigma_0}{L}\bar{\sigma}\bar{\kappa}\mathbf{n} + \frac{\sigma_0}{L}\nabla_s\bar{\sigma} \\ -p\mathbf{n} + 2\mathbf{E}\cdot\mathbf{n} &= \sigma\kappa\mathbf{n} + \nabla_s\sigma \end{aligned} \tag{2.11}$$

We now non-dimensionalize pressure, time, and the strain tensor by

$$p = \frac{\sigma_0}{L}\bar{p},$$
$$t = \frac{L\mu}{\sigma_0}\bar{t},$$
$$\mathbf{E} = \frac{L\mu}{\sigma_0}\bar{\mathbf{E}}.$$

The appearance of the far-field condition (2.6) remains unchanged; however, we non-dimensionalize the far-field velocity by

$$U\bar{\mathbf{u}}_\infty = \frac{1}{2}\begin{pmatrix} \alpha_0 & \beta_0 - \omega_0 \\ \beta_0 + \omega_0 & -\alpha_0 \end{pmatrix} \cdot (L\bar{\mathbf{x}})$$
$$\bar{\mathbf{u}}_\infty = \frac{Q}{2}\begin{pmatrix} 1 & (\beta_0 - \omega_0)/\alpha_0 \\ (\beta_0 + \omega_0)/\alpha_0 & -1 \end{pmatrix} \cdot \bar{\mathbf{x}} \tag{2.12}$$

where the quantities β_0/α_0 and ω_0/α_0 are dimensionless, and we have introduced the *Capillary number* Q

$$Q = \frac{L\alpha_0}{U} = \frac{L\mu\alpha_0}{\sigma_0} \tag{2.13}$$

in terms of which we will characterize the flows investigated in this project. The Capillary number Q represents the ratio of the viscous forces to the surface tension forces.

In the case of the pure strain flow, the shear parameter is zero, $\beta_0 = 0$ and so is the fluid vorticity parameter $\omega_0 = 0$; hence the far-fluid velocity is

$$\bar{\mathbf{u}}_\infty = \frac{Q}{2}(x, -y) \tag{2.14}$$

If case we wish to study the zero surface tension case, these choices in characteristic quantities for non-dimensionalization will not work, since there will be division by zero. It may be preferable to leave the problem in dimensional form.

2.2 The Surfactant Partial Differential Equation

The non-uniformity of surface tension arises from its dependence on the surfactant concentration Γ. This is given by an *equation of state* of the form $\sigma = \sigma(\Gamma)$. Though more complicated equations of state may be used [16, 21], we assume a linear relationship, best for dilute insoluble surfactant concentrations [16]:

$$\sigma = 1 - \beta\Gamma, \tag{2.15}$$

where β is a parameter that controls the degree of sensitivity of the surface tension to changes in the concentration of surfactant. This linear equation of state is simple, widely used [9, 16, 20], and it can be changed without re-modifying the model presented.

As the exterior fluid moves about the bubble, surfactant will be spread across the bubble in a non-uniform layer. Other effects, like diffusion and interface motion change the surfactant distribution as well. An equation for the evolution of surfactant must be coupled with the slow flow equations to complete our mathematical model.

Wong et al. [24] show that the partial differential equation governing the surfactant concentration Γ on the bubble interface C is:

$$\left.\frac{\mathrm{d}\Gamma}{\mathrm{d}t}\right|_C = \frac{\mathrm{d}\mathbf{x}}{\mathrm{d}t} \cdot \nabla_s\Gamma - \nabla_s \cdot (\Gamma\,(\mathbf{u}\cdot\mathbf{s})\mathbf{s}) + \Gamma(\nabla_s \cdot \mathbf{n})(\mathbf{u}\cdot\mathbf{n}) + D_s\nabla_s^2\Gamma, \tag{2.16}$$

where $(\mathbf{u}\cdot\mathbf{s})\mathbf{s} = S\mathbf{s}$ is the tangential interface velocity component, $(\mathbf{u}\cdot\mathbf{n})\mathbf{n} = U\mathbf{n}$ the normal component, κ the local curvature and D_s the diffusivity constant. The term $\left.\frac{\mathrm{d}\Gamma}{\mathrm{d}t}\right|_C$ denotes the partial time derivative of the surfactant concentration on the interface C.

The second term in equation (2.16) describes the influence of the bubble interface motion on the surfactant; it is where the Lagrangian description of the interface is accounted for. The third term describes the convection due to the external fluid with velocity $\mathbf{u}$, motion tangential to the interface, hence the appearance of the S velocity component. The fourth term describes the curvature-driven motion which is perpendicular to the interface, hence the U velocity component, and last is the diffusion term.

The boundary conditions for the surfactant concentration are intuitive: the surfactant is 2π-periodic since the interface C is 2π-periodic.

Surfactant concentration is expressed in units of mass of surfactant per unit of interfacial length and is non-dimensionalized with the uniform concentration of surfactant in the

absence of flow, Γ_0. We have

$$\frac{\Gamma_0\sigma_0}{L\mu}\frac{\mathrm{d}\bar{\Gamma}}{\mathrm{d}\bar{t}}\Big|_C = \frac{\sigma_0\Gamma_0}{L\mu}\frac{\mathrm{d}\bar{\mathbf{x}}}{\mathrm{d}\bar{t}}\cdot\nabla_s\bar{\Gamma} - \frac{\Gamma_0\sigma_0}{L\mu}\nabla_s\cdot(\bar{\Gamma}\,(\bar{\mathbf{u}}\cdot\mathbf{s})\mathbf{s})) - \frac{\Gamma_0\sigma_0}{L\mu}\bar{\Gamma}(\nabla_s\cdot\mathbf{n})(\bar{\mathbf{u}}\cdot\mathbf{n}) + \frac{D_s\Gamma_0}{L^2}\nabla_s^2\bar{\Gamma}$$
$$\frac{\partial\Gamma}{\partial t}\Big|_C = \frac{\partial\mathbf{x}}{\partial t}\cdot\nabla_s\Gamma - \nabla_s\cdot(\Gamma\,(\mathbf{u}\cdot\mathbf{s})\mathbf{s}) - \Gamma(\nabla_s\cdot\mathbf{n})(\mathbf{u}\cdot\mathbf{n}) + \frac{1}{Pe_s}\nabla_s^2\Gamma, \tag{2.17}$$

where Pe_s is the surface Peclet number, a parameter controlling the surfactant diffusion

$$Pe_s = \frac{\sigma_0 L}{\mu D_s}.$$

The fluid velocity on the interface is $\mathbf{u} = U\mathbf{n} + S\mathbf{s}$, where $U = \mathbf{u}\cdot\mathbf{n}$ is the normal velocity component and $S = \mathbf{u}\cdot\mathbf{s}$ is the tangential velocity component. Using $\nabla_s = \mathbf{s}\frac{\partial}{\partial s}$ and $\nabla_s\cdot\mathbf{f} = \mathbf{s}\cdot\frac{\partial}{\partial s}\mathbf{f}$, and the *Frenet Formula* $\frac{\partial\mathbf{s}}{\partial s} = \kappa\mathbf{n}$ and $\frac{\partial\mathbf{n}}{\partial s} = -\kappa\mathbf{s}$ we simplify the terms in equation (2.17):

$$\frac{\mathrm{d}\mathbf{x}}{\mathrm{d}t}\cdot\nabla_s\Gamma = \frac{\mathrm{d}\mathbf{x}}{\mathrm{d}t}\cdot\mathbf{s}\frac{\partial\Gamma}{\partial s}$$
$$\mathbf{s}\cdot\frac{\partial}{\partial s}(\Gamma S\mathbf{s}) = \Gamma S\mathbf{s}\cdot\frac{\partial\mathbf{s}}{\partial s} + \mathbf{s}\cdot\mathbf{s}\frac{\partial(\Gamma S)}{\partial s} = \frac{\partial(\Gamma S)}{\partial s}$$
$$\Gamma(\mathbf{s}\cdot\frac{\partial\mathbf{n}}{\partial s})(\mathbf{u}\cdot\mathbf{n}) = \Gamma(\kappa\mathbf{s}\cdot\mathbf{s})(U) = \kappa U\Gamma$$
$$\frac{1}{Pe_s}\nabla_s^2\Gamma = \frac{1}{Pe_s}\left(\mathbf{s}\cdot\frac{\partial\mathbf{s}}{\partial s}\frac{\partial\Gamma}{\partial s} + \mathbf{s}\cdot\mathbf{s}\frac{\partial^2\Gamma}{\partial s^2}\right) = \frac{1}{Pe_s}\frac{\partial^2\Gamma}{\partial s^2}.$$

Reassembling the terms, we obtain the surfactant equation in the arclength s element

$$\frac{\mathrm{d}\Gamma}{\mathrm{d}t}\Big|_C = \frac{\mathrm{d}\mathbf{x}}{\mathrm{d}t}\cdot\mathbf{s}\frac{\partial\Gamma}{\partial s} - \frac{\partial(\Gamma S)}{\partial s} - \kappa U\Gamma + \frac{1}{Pe_s}\frac{\partial^2\Gamma}{\partial s^2}. \tag{2.18}$$

Non-dimensionalization does not change the general appearance of the equation of state $\sigma = 1 - \beta\Gamma$. We note that since the surface tension σ cannot be a negative value, the equation of state gives bounds for the surfactant concentration, namely $0 \le \Gamma \le \frac{1}{\beta}$. This is a valuable insight, useful as a gauge of accuracy to discard non-physical solutions that might be obtained by inaccurately computed surfactant values.

The surfactant-laden bubble interface problem in a viscous strain flow is now characterized by the three dimensionless parameters Q, Pe_s and β.

2.3 The Biharmonic Equation Theory

It is well-known that the two-dimensional Stokes Flow problem specified in the equations (2.4, 2.5) can be recast in terms of a stream function $\Psi(x,y)$ defined as $u = \partial\Psi/\partial y$, $v = -\partial\Psi/\partial x$ so that $\Psi(x,y)$, and $\mathbf{u} = u + iv$ is the complex velocity. $\Psi(x,y)$ relates to the fluid vorticity $\mathrm{w}(x,y)$ through

$$\nabla^2\Psi = -\mathrm{w} \tag{2.19}$$

and so obeys the *Biharmonic Equation*

$$\nabla^4\Psi = 0. \tag{2.20}$$

There is a complex variable theory for the biharmonic equation that can be exploited to derive analytical solutions [22, 20] or numerical methods [13, 14]. According to it, any plane biharmonic function $\Psi(x,y)$ can be expressed by the Goursat formula as follows:

$$\Psi(x,y) = \mathrm{Re}(\bar{z}\phi(z) + \chi(z)), \tag{2.21}$$

where $\phi(z)$ and $\chi(z)$ are analytic functions of the complex variable $z = x + iy$, and the bar denotes complex conjugation. $\mathrm{Re}(f)$ denotes the real part of the function f, while $\mathrm{Im}(f)$ denotes its imaginary part. We define $\psi(z) = \chi'(z)$, and the analytic functions $\phi(z)$ and $\psi(z)$ are known as the *Goursat Functions.*

Since $\mathbf{u} = (\Psi_y, -\Psi_x)$, we can use (2.19) and (2.4) to find out that

$$\begin{aligned} \mathrm{w}_x &= -\nabla^2\Psi_x = \nabla^2 v = p_y \\ \mathrm{w}_y &= -\nabla^2\Psi_y = -\nabla^2 u = -p_x, \end{aligned}$$

so w and p satisfy the Cauchy-Riemann Equations and $\mathrm{w} + ip$ is an analytic function.

We define the complex quantity $W(x,y) = \bar{z}\phi(z) + \chi(z) = \Psi(x,y) + i\Phi(x,y)$. Then W satisfies the Biharmonic equation $0 = \nabla^2 W = \nabla^2\Psi(x,y) + i\nabla^2\Phi(x,y)$, and it can be shown

$$\begin{aligned} \nabla^2 W &= 4\partial_z\partial_{\bar{z}}(\bar{z}\phi(z) + \chi(z)) \\ &= 4\partial_z(\phi(z)) = 4\phi'(z) \end{aligned} \tag{2.22}$$

But from (2.19), $\nabla^2 W = -\mathrm{w} + i\nabla^2\Phi(x,y) =$, so $-\nabla^2\Phi$ is the harmonic conjugate of w, and thus we must have

$$\nabla^2\Phi(x,y) = -p \tag{2.23}$$

Since $\nabla^2 W = -(\mathrm{w} + ip) = 4\phi'(z)$, the pressure in terms of the Goursat Functions is

$$p = -4\mathrm{Im}(\phi'(z)). \tag{2.24}$$

We can find expressions for all the relevant physical quantities in terms of these Goursat Functions [15]. The velocity term is

$$\begin{aligned} i(u+iv) &= i(\Psi_y - i\Psi_x) \\ &= \Psi_x + i\Psi_y \\ &= \frac{\partial \mathrm{Re}(\bar{z}\phi(z) + \chi(z))}{\partial x} + i\frac{\partial \mathrm{Re}(\bar{z}\phi(z) + \chi(z))}{\partial y} \\ &= \mathrm{Re}(\phi(z) + \bar{z}\phi'(z) + \chi'(z)) + i\mathrm{Im}(\phi(z) - \bar{z}\phi'(z) - \chi'(z)) \\ &= \phi(z) + z\overline{\phi'(z)} + \overline{\chi'(z)}, \\ &= \phi(z) + z\overline{\phi'(z)} + \overline{\psi(z)}, \end{aligned} \tag{2.25}$$

while the stress term is

$$\begin{aligned} e_{11} &= u_x \\ &= -\mathrm{Im}(\bar{z}\phi''(z) + \psi'(z)) \\ e_{12} &= \tfrac{1}{2}(u_y + v_x) \\ &= -\mathrm{Re}(\bar{z}\phi''(z) + \psi'(z)) \\ e_{11} + ie_{12} &= -e_{22} + ie_{21} \\ &= -i(z\overline{\phi''(z)} + \overline{\psi'(z)}). \end{aligned} \tag{2.26}$$

The above notations allow for a reduction of the interface boundary-value problems in Stokes Flow to problems in analytic function theory. That is, we have to find appropriate harmonic functions ϕ and ψ that satisfy the boundary conditions.

First, we look at the stress interface condition. Let ζ be a point on the boundary, $n = n_1 + in_2$ the inward normal, and $s = s_1 + is_2$ the clockwise tangent unit vector, as shown in the Figure 2.1. Then we can write the stress boundary condition (2.11) as

$$-p\delta_{ij}n_j + 2e_{ij}n_j = \sigma\kappa n_i + \frac{\partial\sigma}{\partial s}s_i. \tag{2.27}$$

In terms of the Goursat functions the left hand side is

$$-pn + 2En \equiv 4\mathrm{Im}(\phi')n - 2i(z\overline{\phi''} + \overline{\psi'})\overline{n},$$

Consider a point ζ on the boundary of the domain (see figure 2.1). We know $n = -i\zeta_s$ where s is the arclength traversed in the clockwise direction, so for a point ζ on the boundary, the right hand side becomes

$$\begin{aligned} 4\mathrm{Im}(\phi')n - 2i(\zeta\overline{\phi''} + \overline{\psi'})\overline{n} &= -2(\phi' - \overline{\phi'})\frac{\partial\zeta}{\partial s} + 2(\zeta\overline{\phi''} + \overline{\psi'})\overline{\frac{\delta\zeta}{\delta s}}, \\ &= -2\frac{\partial}{\partial s}(\phi - \zeta\overline{\phi'} - \overline{\psi}) \end{aligned} \tag{2.28}$$

We now substitute $\kappa n = \zeta_{ss}$ and $s = \zeta_s$ into (2.27) and use (2.28) as a point z tends to a point ζ on the interface from above (in direction opposite to n) to obtain:

$$\lim_{z\to\zeta^+} 2\frac{\partial}{\partial s}(\phi - z\overline{\phi'} - \overline{\psi}) = -\sigma\zeta_{ss} - \sigma_s\zeta_s = -\frac{\partial}{\partial s}(\sigma\zeta_s) \qquad \zeta \in C,$$

or simply

$$\lim_{z\to\zeta^+} \frac{\partial}{\partial s}(\phi - z\overline{\phi'} - \overline{\psi}) = -\frac{1}{2}\frac{\partial}{\partial s}(\sigma\zeta_s) \qquad \zeta \in C, \tag{2.29}$$

We can integrate (2.29) w.r.t. s and without loss of generality put the constant to zero:

$$\lim_{z\to\zeta^+} (\phi - z\overline{\phi'} - \overline{\psi}) = -\frac{1}{2}\sigma\zeta_s. \tag{2.30}$$

Both ϕ and ψ, for which we need to find suitable representations, must satisfy (2.30).

On the other hand, these Goursat functions must capture the boundary conditions for the velocity and the pressure as $|z| \to \infty$, as explained in [22]. From (2.24) in this limit it

follows that

$$\phi \sim -\frac{i}{4}p_\infty(t)z + \phi_\infty(z) + B(t) + \mathcal{O}(\frac{1}{|z - z_c|}) \tag{2.31}$$

where the functions p_∞ and $B(t)$ are determined as part of the solution, z_c is an arbitrary point inside the bubble, and we define the function ϕ_∞ as

$$\phi_\infty(z) = -\frac{Q}{4}\frac{w_0}{\alpha_0}z.$$

We note that according to the equations (2.25) and (2.24) the choice of $B(t)$ does not affect the velocity or pressure fields.

Using the equations (2.25) , (2.31) and the far-field velocity (2.12) we can find

$$\psi \sim \psi_\infty(z) - \overline{B(t)} + \mathcal{O}(\frac{1}{|z - z_c|^2}) \tag{2.32}$$

where the function ψ_∞ is

$$\psi_\infty(z) = -i\frac{Q}{2}(1 - i\frac{\beta_0}{\alpha_0})z.$$

Again, we state that ϕ_∞ and ψ_∞ are suitably chosen analytic functions that according to (2.25) satisfy

$$\phi_\infty(z) + z\overline{\phi'_\infty(z)} + \overline{\psi_\infty(z)} = i(u_\infty + iv_\infty) \tag{2.33}$$

and $\mathbf{u}_\infty$, the far-field velocity is

$$u_\infty + iv_\infty = \frac{Q}{2}\left((1 + i\frac{\beta_0}{\alpha_0})\overline{z} + i\frac{\omega_0}{\alpha_0}z\right).$$

For a pure straining flow, the strain parameters are $\beta_0 = 0$, $w_0 = 0$. This gives us the following far-field values

$$\begin{aligned} u_\infty + iv_\infty &= \frac{Q}{2}\overline{z} \\ \phi_\infty(z) &= 0 \\ \psi_\infty(z) &= -i\frac{Q}{2}z. \end{aligned} \tag{2.34}$$

2.4 The Sherman-Lauricella Integral Equations

Greengard et al. [10] use the Sherman-Lauricella equation to formulate integral equation methods for solving a variety of boundary-value Stokes Flow problems. Kropinski [13] uses these integral equations for researching interface problems in Stokes Flow, in bounded or unbounded fluid domains.

We outline here a derivation of the integral equation that is associated with interface problems in Stokes Flow in unbounded domains, since it is the problem at hand. The $\phi(z)$ and $\psi(z)$ Goursat functions that satisfy the boundary conditions of our problem are assumed [10, 13, 14] to have the following integral representations:

$$\begin{aligned}\phi(z) &= \frac{1}{2\pi i}\oint_C \frac{\omega(\xi,t)}{\xi - z}d\xi + \oint \omega(\xi,t)ds - \frac{i}{4}p_\infty(t)z + \phi_\infty(z),\\ \psi(z) &= \frac{1}{2\pi i}\oint_C \frac{-\overline{\omega(\xi,t)}d\xi + \omega(\xi,t)d\bar{\xi}}{\xi - z} - \frac{1}{2\pi i}\oint_C \frac{\bar{\xi}\omega(\xi,t)}{(\xi - z)^2}d\xi + \psi_\infty(z),\end{aligned} \tag{2.35}$$

where $\omega(\xi,t)$ is an unknown complex density on the boundary C, and $\oint_C$ is used to denote principal value integrals.

If we let z tend to a point ζ on the interface C, when substituting the representations (2.35) into the equation (2.30) , and use the formula for the limiting values of Cauchy-type integrals, we obtain the Sherman-Lauricella integral equation

$$\begin{aligned}\omega(\zeta,t) + \frac{1}{2\pi i}\oint_C \omega(\xi,t)d\ln\frac{\xi-\zeta}{\bar{\xi}-\bar{\zeta}} + \frac{1}{2\pi i}\oint_C \overline{\omega(\xi,t)}d\frac{\xi-\zeta}{\bar{\xi}-\bar{\zeta}} + \int \omega(\xi,t)ds\\ = -\frac{\sigma}{2}\frac{\partial\zeta}{\partial s} + \frac{i}{2}p_\infty\zeta - \left(\phi_\infty(\zeta) - \zeta\overline{\phi'_\infty(\zeta)} - \overline{\psi_\infty(\zeta)}\right).\end{aligned} \tag{2.36}$$

The pressure term representations must be chosen so that the integral equations are well-conditioned, so the far-field pressure $p_\infty(t)$ is chosen to be

$$p_\infty(t) = -\frac{2}{\pi}Re\oint_C \frac{\omega(\xi,t)}{(\xi - z_c)^2}d\xi \tag{2.37}$$

where z_c is an arbitrary point inside the bubble. The above fixes a value for the pressure at (an arbitrarily chosen) value for z_c. The gas pressure inside the bubble then is

$$0 = p = p_\infty(t) + \frac{2}{\pi}Re\oint_C \frac{\omega(\xi,t)}{(\xi - z_c)^2}d\xi.$$

For the fluid velocity on the interface, when substituting (2.35) into the kinematic condition (2.25), we have the integral representation

$$\begin{aligned} u+iv &= -i\lim_{z\to\zeta}(\phi + z\overline{\phi'} + \overline{\psi}) \\ &= -\frac{1}{2\pi}\oint_C \omega(\xi,t)\left(\frac{d\xi}{\xi-\zeta} + \frac{d\overline{\xi}}{\overline{\xi}-\overline{\zeta}}\right) + \frac{1}{2\pi}\oint_C \overline{\omega(\xi,t)}d(\frac{\xi-\zeta}{\overline{\xi}-\overline{\zeta}}) + u_\infty + iv_\infty. \end{aligned} \tag{2.38}$$

The value of the complex weight $\omega(\zeta,t)$ is found from the solution of the Sherman-Lauricella equation (2.36), and then it is used to find the velocity according to (2.38). The velocity is in turn used to evolve the interface via the kinematic condition (2.10).

To find the value of $\omega(\zeta,t)$ from (2.36), the equation needs to be invertible and this seems a daunting task, given that the integral kernels are singular. However, it is a possible task, as was demonstrated in [13] when substituting the simple case $\xi-\zeta = re^{i\nu}$. Assuming the contours C are themselves smooth, the integral equation ensuing after the substitution is a Fredholm equation of the second kind with smooth kernels, hence the Fredholm alternative applies and the equation is invertible for $\omega(\zeta,t)$. We will not elaborate here on the invertibility of the general case of (2.36), but a complete proof of it can be found in [17].

We can further simplify the singular kernels of the integrals by noting that

$$\begin{aligned} d\frac{\xi-\zeta}{\overline{\xi}-\overline{\zeta}} &= \frac{d\xi}{\xi-\zeta} - \frac{(\xi-\zeta)d\overline{\xi}}{(\overline{\xi}-\overline{\zeta})^2} \\ d\ln\frac{\xi-\zeta}{\overline{\xi}-\overline{\zeta}} &= \left(\frac{\overline{\xi}-\overline{\zeta}}{\xi-\zeta}\right)\left(\frac{d\xi}{\overline{\xi}-\overline{\zeta}} - \frac{(\xi-\zeta)d\overline{\xi}}{(\overline{\xi}-\overline{\zeta})^2}\right) = \frac{d\xi}{\xi-\zeta} - \frac{d\overline{\xi}}{\overline{\xi}-\overline{\zeta}}. \end{aligned}$$

The Sherman-Lauricella integral equations now become

$$\begin{aligned} &\omega(\zeta,t) + \frac{1}{2\pi i}\int_C \omega(\xi,t)\left(\frac{d\xi}{\xi-\zeta} - \frac{d\overline{\xi}}{\overline{\xi}-\overline{\zeta}}\right) + \frac{1}{2\pi i}\int_C \overline{\omega(\xi,t)}\left(\frac{d\xi}{\xi-\zeta} - \frac{(\xi-\zeta)d\overline{\xi}}{(\overline{\xi}-\overline{\zeta})^2}\right) \\ &\quad + \int \omega(\xi,t)ds = -\frac{\sigma}{2}\frac{\partial\zeta}{\partial s} + \frac{i}{2}p_\infty\zeta - \left(\phi_\infty(\zeta) - \zeta\overline{\phi'_\infty(\zeta)} - \overline{\psi_\infty(\zeta)}\right) \end{aligned} \tag{2.39}$$

$$\begin{aligned} u+iv = &-\frac{1}{2\pi}\oint_C \omega(\xi,t)\left(\frac{d\xi}{\xi-\zeta} + \frac{d\overline{\xi}}{\overline{\xi}-\overline{\zeta}}\right) + \frac{1}{2\pi}\oint_C \overline{\omega(\xi,t)}\left(\frac{d\xi}{\xi-\zeta} - \frac{(\xi-\zeta)d\overline{\xi}}{(\overline{\xi}-\overline{\zeta})^2}\right) \\ &+ u_\infty + iv_\infty, \end{aligned} \tag{2.40}$$

and this is the form we will use for the remainder of this thesis.

Chapter 3

The Equal Arclength Frame

Many interface tracking methods, (e.g. see [18]) follow the time integration of the equations we described in the last chapter. However, the Lagrangian description of the problem, in which the interface marker points are advected by the fluid velocity, leads to point clustering at regions of high curvature, or inadequate interface resolution; hence it is not the best method for long-time interface simulations. The stability constraint on the time-step is $\Delta t = \mathcal{O}(\Delta \overline{s})$, where $\Delta \overline{s} = min(\Delta s)$ is the smallest distance between the marker points [13].

A remedy to the problem was proposed by Hou et al. in [11]. They noted that since the shape of the interface is determined solely by the normal component of the velocity $U = \mathbf{u} \cdot \mathbf{n}$ in the kinematic condition (2.10), a tangential component which bears no consequence in the motion itself can be introduced:

$$\frac{\mathrm{d}\mathbf{x}}{\mathrm{d}t} = U\mathbf{n} + T\mathbf{s}. \tag{3.1}$$

The component T is chosen so that it dynamically maintains the marker points at equal arclength spacing. This is called the equal arclength frame. The formulation resolves the issue of grid point clustering and eases the stability constraint.

When non-constant surface tension is involved, the surfactant equation has to be solved as well. The convective-diffusive surfactant equation is stiff and a linear stability analysis gives a $\Delta t = \mathcal{O}((\Delta \overline{s})^2)$ time-stepping restriction for explicit methods. To integrate the equation, we use Implicit-Explicit methods [3, 4], which treat the stiff terms implicitly. The time-stepping for it is then linear with respect to the mesh. The linearity is reinforced by the choice of T, and the time step is $\Delta t = \mathcal{O}(\Delta s)$ since Δs is uniform throughout the interface.

3.1 The Interface Motion

We explain here in detail how Kropinski in [13, 14] successfully applied the equal arclength frame to the Stokes Flow problem in two dimensions.

A clockwise parametrization on the interface is introduced, as in figure 2.1, so that the interface is described by the variable $\zeta(\alpha,t) = x(\alpha,t) + iy(\alpha,t)$ where $\alpha \in [0,2\pi]$. The normal and the tangent are then given by:

$$n = -i\frac{\zeta_\alpha}{s_\alpha} = -ie^{i\theta}, s = \frac{\zeta_\alpha}{s_\alpha} = e^{i\theta}$$

where s is the arclength, θ the angle tangent to the interface and $s_\alpha = |\zeta_\alpha|$. One can then rewrite (3.1) as:

$$\frac{\mathrm{d}\zeta}{\mathrm{d}t} = -Ui\frac{\zeta_\alpha}{s_\alpha} + T\frac{\zeta_\alpha}{s_\alpha} = -Uie^{i\theta} + Te^{i\theta}. \tag{3.2}$$

In terms of the arclength s and the tangent angle, we have $\zeta_\alpha = s_\alpha e^{i\theta}$. Differentiating with respect to t, we obtain

$$\frac{\mathrm{d}\zeta_\alpha}{\mathrm{d}t} = s_{\alpha t}e^{i\theta} + s_\alpha\theta_t ie^{i\theta},$$

The derivative of (3.2) with respect to α is

$$\frac{\mathrm{d}\zeta_\alpha}{\mathrm{d}t} = (U\theta_\alpha + T_\alpha)e^{i\theta} + (T\theta_\alpha - U_\alpha)ie^{i\theta}.$$

Equating the right-hand sides of the two above equations, one obtains the evolution equations for s_α and θ

$$\begin{aligned}\frac{\mathrm{d}s_\alpha}{\mathrm{d}t} &= U\theta_\alpha + T_\alpha \\ \frac{\mathrm{d}\theta}{\mathrm{d}t} &= \frac{1}{s_\alpha}(T\theta_\alpha - U_\alpha).\end{aligned} \tag{3.3}$$

For an equal arclength spacing, s_α needs to be uniform throughout the curve, thus

$$s_\alpha(\alpha,t) = \frac{1}{2\pi}\int_0^{2\pi} s_\alpha(\alpha',t)d\alpha' \tag{3.4}$$

which is the average over a period.

The equal arclength frame is reinforced by a particular choice of T. This T is found by differentiating (3.4) and using (3.3)

$$T(\alpha,t) = T(0,t) - \int_0^\alpha U\theta_{\alpha'}d\alpha' + \frac{\alpha}{2\pi}\int_0^{2\pi} U\theta_{\alpha'}d\alpha'. \tag{3.5}$$

If s_α satisfies (3.4) initially, then the choice of T above ensures the equal arclength constraint in time.

The evolution equation for s_α in equal-spacing can be now recast as

$$\frac{\mathrm{d}s_\alpha}{\mathrm{d}t} = \frac{1}{2\pi}\int_0^{2\pi} U\theta_{\alpha'}d\alpha'. \tag{3.6}$$

3.2 Modification of the Surfactant Equation

We previously explained that the surfactant dynamics on the bubble interface is governed by the following non-dimensional partial differential equation

$$\frac{\mathrm{d}\Gamma}{\mathrm{d}t}\Big|_C = \frac{\mathrm{d}\zeta}{\mathrm{d}t}\cdot\mathbf{s}\frac{\partial\Gamma}{\partial s} - \frac{\partial(\Gamma S)}{\partial s} - \kappa U\Gamma + \frac{1}{Pe_s}\frac{\partial^2\Gamma}{\partial s^2},$$

where ζ is a point on the interface.

We noted in the last chapter that the velocity on the interface is computed by solving the integral equation (2.36). This complex velocity is written as $u + iv = U\mathbf{n} + S\mathbf{s}$, where $U = \mathbf{u}\cdot\mathbf{n}$ is the normal component and $S = \mathbf{u}\cdot\mathbf{s}$ is the tangential component. On the other hand we have equation (3.1) that describes the kinematic condition in the new formulation, namely $\frac{\mathrm{d}\zeta}{\mathrm{d}t} = U\mathbf{n} + T\mathbf{s}$. We substitute these in the equation for the surfactant

$$\frac{\mathrm{d}\Gamma}{\mathrm{d}t}\Big|_C = (U\mathbf{n} + T\mathbf{s})\cdot\mathbf{s}\frac{\partial\Gamma}{\partial s} - \frac{\partial(\Gamma S)}{\partial s} - \kappa U\Gamma + \frac{1}{Pe_s}\frac{\partial^2\Gamma}{\partial s^2}. \tag{3.7}$$

The second term can be simplified to

$$(U\mathbf{n} + T\mathbf{s})\cdot\mathbf{s}\frac{\partial\Gamma}{\partial s} = T\frac{\partial\Gamma}{\partial s},$$

hence the surfactant equation in the s element now becomes

$$\frac{\mathrm{d}\Gamma}{\mathrm{d}t}\Big|_C = T\frac{\partial\Gamma}{\partial s} - \frac{\partial(\Gamma S)}{\partial s} - \kappa U\Gamma + \frac{1}{Pe_s}\frac{\partial^2\Gamma}{\partial s^2}.$$

For the α-parametrization of the equation we substitute $\frac{\partial}{\partial s} = \frac{1}{s_\alpha}\frac{\partial}{\partial \alpha}$ and $\kappa = \frac{\partial \theta}{\partial s} = \frac{1}{s_\alpha}\frac{\partial \theta}{\partial \alpha}$ and modify the terms of the surfactant equation as

$$\begin{aligned} T\frac{\partial \Gamma}{\partial s} &= \frac{T}{s_\alpha}\frac{\partial \Gamma}{\partial \alpha} \\ \frac{\partial(\Gamma S)}{\partial s} &= \frac{1}{s_\alpha}\frac{\partial(\Gamma S)}{\partial \alpha} \\ \kappa U\Gamma &= \frac{1}{s_\alpha}U\Gamma\frac{\partial \theta}{\partial \alpha} \\ \frac{1}{Pe_s}\frac{\partial^2 \Gamma}{\partial s^2} &= \frac{1}{Pe_s}\frac{1}{s_\alpha}\frac{\partial}{\partial \alpha}\left(\frac{1}{s_\alpha}\frac{\partial \Gamma}{\partial \alpha}\right). \end{aligned}$$

The interface is equi-parametrized and $s_{\alpha\alpha} = 0$, so the last surfactant term is

$$\frac{1}{Pe_s}\frac{1}{s_\alpha}\frac{\partial}{\partial \alpha}\left(\frac{1}{s_\alpha}\frac{\partial \Gamma}{\partial \alpha}\right) = \frac{1}{Pe_s}\frac{1}{s_\alpha^2}\frac{\partial^2 \Gamma}{\partial \alpha^2}.$$

Assembling all the terms, we obtain the surfactant equation in its final form

$$\left.\frac{\mathrm{d}\Gamma}{\mathrm{d}t}\right|_C = \frac{T}{s_\alpha}\frac{\partial \Gamma}{\partial \alpha} - \frac{1}{s_\alpha}\frac{\partial(\Gamma S)}{\partial \alpha} - \frac{1}{s_\alpha}U\Gamma\frac{\partial \theta}{\partial \alpha} + \frac{1}{Pe_s}\frac{1}{s_\alpha^2}\frac{\partial^2 \Gamma}{\partial \alpha^2} \tag{3.8}$$

where $\Gamma = \Gamma(\alpha, t)$, $s_\alpha = s_\alpha(t)$, $T = T(\alpha, t)$, $U = U(\alpha, t)$ and $S = S(\alpha, t)$.

The above equation is now solved together with the interface evolution equations described in the previous section.

The surfactant 2π-periodicity boundary condition is

$$\Gamma(\alpha, t) = \Gamma(\alpha + 2\pi, t).$$

Since we are interested in the insoluble surfactant problem, i.e zero surfactant flux into the outside fluid, the total amount of surfactant on the bubble surface is fixed. Hence the total amount of surfactant on the interface is not changing in time

$$\frac{d}{dt}\int_0^{2\pi} \Gamma(\alpha', t) s_{\alpha'} d\alpha' = 0. \tag{3.9}$$

This is a rather useful constraint and will be utilized to check the accuracy of the numerical solutions.

3.3 The Parametrization of the Integral Equations

For completeness, we describe how the Integral Equations transfer to the α-parametrization.

The complex weight $\omega(\zeta,t)$ featuring in the integral equations is found at every point $\zeta(\alpha,t)$ on the interface and we write $\omega(\zeta,t) = \omega(\alpha,t)$. The Sherman-Lauricella integral equation (2.39) is written as

$$\begin{aligned}
&\omega(\alpha,t) + \frac{1}{2\pi i}\int_0^{2\pi} \omega(\alpha',t)\left(\frac{\zeta_{\alpha'}(\alpha',t)}{\zeta(\alpha',t)-\zeta(\alpha,t)} - \frac{\overline{\zeta}_{\alpha'}(\alpha',t)}{\overline{\zeta}(\alpha',t)-\overline{\zeta}(\alpha,t)}\right)d\alpha' \\
&\quad + \frac{1}{2\pi i}\int_0^{2\pi} \overline{\omega(\alpha',t)}\left(\frac{\zeta_{\alpha'}(\alpha',t)}{\zeta(\alpha',t)-\zeta(\alpha,t)} - \frac{(\zeta(\alpha',t)-\zeta(\alpha,t))\overline{\zeta}_{\alpha'}(\alpha',t)}{(\overline{\zeta}(\alpha',t)-\overline{\zeta}(\alpha,t))^2}\right)d\alpha' \\
&\quad + \int_0^{2\pi} \omega(\alpha',t)s_\alpha(t)d\alpha' \\
&\quad = -\frac{\sigma(\alpha,t)}{2}\frac{\zeta_\alpha(\alpha,t)}{s_\alpha(t)} + \frac{i}{2}p_\infty(t)\zeta(\alpha,t) - \left(\phi_\infty - \zeta(\alpha,t)\overline{\phi'_\infty} - \overline{\psi_\infty}\right)
\end{aligned} \tag{3.10}$$

where we remind the reader that the far-field pressure term is

$$p_\infty(t) = -\frac{2}{\pi}\mathrm{Re}\int_0^{2\pi}\frac{\omega(\alpha',t)\zeta_{\alpha'}(\alpha',t)}{(\zeta(\alpha',t)-z_c)^2}d\alpha' \tag{3.11}$$

and we recall the values of ϕ_∞ and ψ_∞ from (2.34) for the pure strain flow to find

$$\phi_\infty - \zeta(\alpha,t)\overline{\phi'_\infty} - \overline{\psi_\infty} = -i\frac{Q}{2}\overline{\zeta(\alpha,t)}. \tag{3.12}$$

We parametrize the complex velocity integral equation (2.40) in a similar way, and we obtain

$$\begin{aligned}
u+iv = &-\frac{1}{2\pi}\int_0^{2\pi}\omega(\alpha',t)\left(\frac{\zeta_{\alpha'}(\alpha',t)}{\zeta(\alpha',t)-\zeta(\alpha,t)} + \frac{\overline{\zeta}_{\alpha'}(\alpha',t)}{\overline{\zeta}(\alpha',t)-\overline{\zeta}(\alpha,t)}\right)d\alpha' \\
&+ \frac{1}{2\pi}\int_0^{2\pi}\overline{\omega(\alpha',t)}\left(\frac{\zeta_{\alpha'}(\alpha',t)}{\zeta(\alpha',t)-\zeta(\alpha,t)} - \frac{(\zeta(\alpha',t)-\zeta(\alpha,t))\overline{\zeta}_{\alpha'}(\alpha',t)}{(\overline{\zeta}(\alpha',t)-\overline{\zeta}(\alpha,t))^2}\right)d\alpha' \\
&+ u_\infty + iv_\infty
\end{aligned} \tag{3.13}$$

where the far field velocity for pure strain flows (2.34) is

$$u_\infty + iv_\infty = \frac{Q}{2}\overline{\zeta(\alpha,t)}. \tag{3.14}$$

For simplicity, we will write the Sherman-Lauricella integral equation (3.10) and the complex velocity integral equation (3.13) as

$$\omega(\alpha,t)+\int_0^{2\pi}\omega(\alpha',t)K_1\left(\zeta(\alpha,t),\zeta(\alpha',t)\right)d\alpha'+\int_0^{2\pi}\overline{\omega(\alpha',t)}K_2\left(\zeta(\alpha,t),\zeta(\alpha',t)\right)d\alpha' + \int_0^{2\pi}\omega(\alpha',t)s_\alpha(t)d\alpha' = -\frac{\sigma(\alpha,t)}{2}\frac{\zeta_\alpha(\alpha,t)}{s_\alpha(t)}+\frac{i}{2}p_\infty(t)\zeta(\alpha,t)-\left(\phi_\infty-\zeta(\alpha,t)\overline{\phi'_\infty}-\overline{\psi_\infty}\right) \tag{3.15}$$

$$u+iv=\int_0^{2\pi}\omega(\alpha',t)K_1'\left(\zeta(\alpha,t),\zeta(\alpha',t)\right)d\alpha'+i\int_0^{2\pi}\overline{\omega(\alpha',t)}K_2\left(\zeta(\alpha,t),\zeta(\alpha',t)\right)d\alpha' + u_\infty+iv_\infty \tag{3.16}$$

where we have suitably defined the integral kernels K_1, K_2 and K_1' to be

$$K_1\left(\zeta(\alpha,t),\zeta(\alpha',t)\right)=\frac{1}{2\pi i}\left(\frac{\zeta_{\alpha'}(\alpha',t)}{\zeta(\alpha',t)-\zeta(\alpha,t)}-\frac{\overline{\zeta}_{\alpha'}(\alpha',t)}{\overline{\zeta}(\alpha',t)-\overline{\zeta}(\alpha,t)}\right)$$

$$K_2\left(\zeta(\alpha,t),\zeta(\alpha',t)\right)=\frac{1}{2\pi i}\left(\frac{\zeta_{\alpha'}(\alpha',t)}{\zeta(\alpha',t)-\zeta(\alpha,t)}-\frac{(\zeta(\alpha',t)-\zeta(\alpha,t))\overline{\zeta}_{\alpha'}(\alpha',t)}{(\overline{\zeta}(\alpha',t)-\overline{\zeta}(\alpha,t))^2}\right)$$

$$K_1'\left(\zeta(\alpha,t),\zeta(\alpha',t)\right)=\frac{1}{2\pi}\left(\frac{\zeta_{\alpha'}(\alpha',t)}{\zeta(\alpha',t)-\zeta(\alpha,t)}+\frac{\overline{\zeta}_{\alpha'}(\alpha',t)}{\overline{\zeta}(\alpha',t)-\overline{\zeta}(\alpha,t)}\right).$$

Finally, we remind the reader how the velocity components U and S are obtained from the complex velocity $u+iv$ by

$$u+iv=U\mathbf{n}+S\mathbf{s}=-Ui\frac{\zeta_\alpha}{s_\alpha}+S\frac{\zeta_\alpha}{s_\alpha};$$

therefore,

$$U(\alpha,t)=-\mathrm{Im}\left(\frac{s_\alpha(\alpha,t)}{\zeta_\alpha(\alpha,t)}(u+iv)\right) \tag{3.17}$$

$$S(\alpha,t)=\mathrm{Re}\left(\frac{s_\alpha(\alpha,t)}{\zeta_\alpha(\alpha,t)}(u+iv)\right). \tag{3.18}$$

These velocity components can now be used in the computation of the other quantities, for example interface position ζ from (3.2), the equi-parametrization velocity T from (3.5), the geometry variables s_α and θ from (3.3), the surfactant concentration Γ from (3.8) and the surface tension σ from (2.15).

3.4 The System of Time Evolution Equations

We summarize here all the equations for the bubble in a linear strain flow.

$$\frac{\mathrm{d}\zeta}{\mathrm{d}t} = -Ui\frac{\zeta_\alpha}{s_\alpha} + T\frac{\zeta_\alpha}{s_\alpha} \tag{3.19}$$

$$\frac{\mathrm{d}s_\alpha}{\mathrm{d}t} = \frac{1}{2\pi}\int_0^{2\pi} U\theta_{\alpha'}d\alpha' \tag{3.20}$$

$$T(\alpha) = T(0) - \int_0^\alpha U(\alpha')\theta_{\alpha'}(\alpha')d\alpha' + \frac{\alpha}{2\pi}\int_0^{2\pi} U(\alpha',t)\theta_{\alpha'}(\alpha',t)d\alpha' \tag{3.21}$$

$$U = -\mathrm{Im}\left(\frac{s_\alpha}{\zeta_\alpha}(u+iv)\right) \tag{3.22}$$

$$S = \mathrm{Re}\left(\frac{s_\alpha}{\zeta_\alpha}(u+iv)\right) \tag{3.23}$$

$$u+iv = \int_0^{2\pi}\omega(\alpha')K_1'\left(\zeta(\alpha),\zeta(\alpha')\right)d\alpha' + i\int_0^{2\pi}\overline{\omega(\alpha')}K_2\left(\zeta(\alpha),\zeta(\alpha')\right)d\alpha' + \frac{Q}{2}\bar{\zeta} \tag{3.24}$$

$$\begin{aligned}\omega + \int_0^{2\pi}\omega(\alpha')K_1\left(\zeta(\alpha),\zeta(\alpha')\right)d\alpha' + \int_0^{2\pi}\overline{\omega(\alpha')}K_2\left(\zeta(\alpha),\zeta(\alpha')\right)d\alpha' + \int_0^{2\pi}\omega s_\alpha d\alpha' \\ = -\frac{\sigma}{2}\frac{\zeta_\alpha}{s_\alpha} + \frac{i}{2}p_\infty(t)\zeta + i\frac{Q}{2}\bar{\zeta}\end{aligned} \tag{3.25}$$

$$p_\infty(t) = -\frac{2}{\pi}\mathrm{Re}\int_0^{2\pi}\frac{\omega\xi_{\alpha'}}{(\xi(\alpha')-z_c)^2}d\alpha' \tag{3.26}$$

$$\sigma = 1 - \beta\Gamma(\alpha,t) \tag{3.27}$$

$$\frac{\partial\Gamma}{\partial t} = \frac{T}{s_\alpha}\frac{\partial\Gamma}{\partial\alpha} - \frac{1}{s_\alpha}\frac{\partial(\Gamma S)}{\partial\alpha} - \frac{1}{s_\alpha}U\Gamma\frac{\partial\theta}{\partial\alpha} + \frac{1}{Pe_s}\frac{1}{s_\alpha^2}\frac{\partial^2\Gamma}{\partial\alpha^2} \tag{3.28}$$

where $\zeta = \zeta(\alpha,t)$, $s_\alpha = s_\alpha(t)$, $\theta = \theta(\alpha,t)$, $T = T(\alpha,t)$, $U = U(\alpha,t)$, $S = S(\alpha,t)$, $u+iv = (u+iv)(\alpha,t)$, $\omega = \omega(\alpha,t)$, $p_\infty = p_\infty(t)$, $\sigma = \sigma(\alpha,t)$, and $\Gamma = \Gamma(\alpha,t)$.

We have to supply $\zeta(\alpha,0)$, $\Gamma(\alpha,0)$, β, Q, Pe_s, z_c, and the rest of the quantities can be evolved in time according to the above equations.

Chapter 4

The Numerical Implementation

In this chapter we explain how to numerically implement the problem of a bubble in a pure strain flow described by the equations (3.19-3.28). The first section explains how the spatial derivatives are numerically discretized. The second explains how the integral equations are discretized. The third section explains the numerical integration methods for the interface equations, while the final section deals with the numerical integration method for the surfactant concentration.

4.1 Spectral Description of the Functions

We start with an initial bubble interface, specified at N even points. The *Equi-arclength Parametrization* of the marker points on the interface is obtained by following the procedure outlined in [11], which involves solving, by Newton's Method, a sequence of nonlinear equations for the N marker points at equal arclength intervals. Then the interface position ζ is uniformly discretized in α, where $\Delta\alpha = 2\pi/N$ is the mesh spacing, $\alpha_j = 2\pi j/N$, $1 \leq j \leq N$ and f_j is a function's value at the marker point.

The interface ζ is 2π-periodic, and so are the velocities U, T, S, the arclength element s_α, angle θ, and the surfactant concentration Γ. The geometry of the problem naturally suggests the use of Fast Fourier Transforms in computations. By representing the distribution of these functions in Fourier space, computing spatial derivatives is reduced to multiplication. Next we explain how the methods of *Fourier Differentiation* and *Fourier Integration* are numerically implemented.

Let the function f be discretized at the N marker points α_j, and denote these points by f_j. Let its Discrete Fourier Transform be

$$\hat{f}_k = \sum_{j=1}^{N} f_j e^{-ik\alpha_j}, \quad \text{for} \quad k = -\frac{N}{2}+1, ..., \frac{N}{2}.$$

Derivatives of order m, denoted by $D_h^m f_j$, are given at the marker points as follows

$$f_j = D_h^0 f_j = \frac{1}{N} \sum_{k=-N/2+1}^{N/2} \hat{f}_k e^{ik\alpha_j} \quad \text{for} \quad j = 1, ..., N,$$

$$\partial_\alpha^m f_j = D_h^m f_j = \frac{1}{N} \sum_{k=-N/2+1}^{N/2} (ik)^m \hat{f}_k e^{ik\alpha_j} \quad \text{for} \quad j = 1, ..., N,$$

while the integrals, with the integration constant denoted as F_0, are computed as

$$\int_0^{\alpha_j} f(\alpha) d\alpha = F_0 + \hat{f}_0 \alpha_j + \sum_{k=-N/2, k\neq 0}^{N/2-1} \frac{\hat{f}_k}{ik} e^{ik\alpha_j}$$

The Fast Fourier Transform is a computationally efficient way to calculate the Discrete Fourier Transform and its inverse as given above with N a power of two, with a $\mathcal{O}(N \log_2 N)$ cost. The computations are spectrally accurate, meaning convergence is exponential. They can therefore be used to produce highly accurate computations.

We must note however that accuracy is lost as a function becomes more complex. In long-time computations, a function may become underresolved. In that case, we double the number of points using the *Fourier Interpolation Method*, which effectively pads the spectrum with N zeros as outlined below:

$$\hat{g}_k = \begin{cases} 2\hat{f}_{k+N/2} & \text{for} \quad k = -N+1, ..., -\frac{N}{2}, \\ 0 & \text{for} \quad k = -\frac{N}{2}+1, ..., \frac{N}{2}, \\ 2\hat{f}_{k-N/2} & \text{for} \quad k = \frac{N}{2}+1, ..., N, \end{cases}$$

$$g_j = \frac{1}{2N} \sum_{k=-N+1}^{N} \hat{g}_k e^{ik\alpha'_j} \quad \text{for} \quad \alpha'_j = \frac{2\pi j}{N}, j = 1, ..., 2N.$$

Now g is f is effectively interpolated at $2N$ points, with a spectrally accurate calculation.

4.2 Discretization of the Integral Equations

We mentioned before that to discretize Sherman-Lauricella integral equations we will follow the approach used by Kropinski in [13, 14]. We briefly outline here the main points of the approach and explain how it is achieved numerically.

First, the number of points on the interface is doubled to $N' = 2N$ and the step length is defined as $h = 2\pi/N'$. At each point ζ_j, we have to find the associated ω_j, by solving the equations. Let $[\zeta_\alpha]_j$ denote the pseudospectral derivative of ζ w.r.t. α. The discretization of the Sherman-Lauricella integral equation then reads

$$\omega_j + \sum_{i=1}^{N'} K_1(\zeta_j, \zeta_i) w_i + \sum_{i=1}^{N'} K_2(\zeta_j, \zeta_i)\overline{w_i} + h\sum_{i=1}^{N'} \omega_i [s_\alpha]_i = g_j \tag{4.1}$$

where

$$g_j = -\frac{\sigma_j}{2}\frac{[\zeta_\alpha]_j}{|[\zeta_\alpha]_j|} - i\frac{h}{2\pi}\zeta_j \sum_{i=1}^{N'} \mathrm{Re}\left(\frac{\omega_i [\zeta_\alpha]_i}{(\zeta_i - z_c)^2}\right) - \left(\phi_\infty(\zeta_j) - \zeta_j\overline{\phi'_\infty(\zeta_j)} - \overline{\phi'_\infty(\zeta_j)}\right)$$

The kernels $K_1(\zeta_j, \zeta_i)$ and $K_2(\zeta_j, \zeta_i)$ are given by

$$K_1(\zeta_j, \zeta_i) = \frac{h}{2\pi i}\left(\frac{[\zeta_\alpha]_i}{\zeta_i - \zeta_j} - \frac{\overline{[\zeta_\alpha]_i}}{\overline{\zeta_i - \zeta_j}}\right)$$

$$K_2(\zeta_j, \zeta_i) = \frac{h}{2\pi i}\left(\frac{[\zeta_\alpha]_i}{\overline{\zeta_i - \zeta_j}} - \frac{\overline{[\zeta_\alpha]_i}(\zeta_i - \zeta_j)}{(\overline{\zeta_i - \zeta_j})^2}\right)$$

When $\zeta_j = \zeta_i$, K_1 and K_2 should be replaced by the limits, as explained in [10, 13],

$$K_1(\zeta_j, \zeta_j) = \frac{h}{2\pi}\kappa_j |[\zeta_\alpha]_j|$$

$$K_2(\zeta_j, \zeta_j) = \frac{h}{2\pi}\kappa_j \frac{[\zeta_\alpha]_j^2}{|[\zeta_\alpha]_j|}$$

where κ is the curvature, calculated pseudospectrally using

$$\kappa = \frac{x_\alpha y_{\alpha\alpha} - x_{\alpha\alpha} y_\alpha}{(x_\alpha^2 + y_\alpha^2)^{3/2}}. \tag{4.2}$$

The equation (4.1) for ω results in a linear system for ω

$$\vec{\omega} + [K_1]\vec{\omega} + [K_2]\vec{\overline{\omega}} + [H]\vec{\omega} = \vec{g}$$
$$([I_{N'}] + [K_1] + [K_2]\mathcal{C} + [H])\,\vec{\omega} = \vec{g}$$

where $[K_1]$, $[K_2]$ and $[H]$ denote $N' \times N'$ matrices with the entries $[K_1]_{ml} = K_1(\zeta_l, \zeta_m)$ and $[K_2]_{ml} = K_2(\zeta_l, \zeta_m)$, $[H]_{ml} = hs_\alpha$, while $\mathcal{C}$ denotes the complex conjugation operator.

The system is solved iteratively using the *Generalized Minimum Residual Method*, or GMRES, until subsequent iterations are within a certain specified tolerance. We stress that the iterations are numerically convergent as the Sherman-Lauricella integral equations are Fredholm Integral equations of the Second Kind; and in fact, the number of iterations are guaranteed to be bounded independently of N [10, 13].

The matrices $[K_1]$ and $[K_2]$ are dense; the most computational work in each iteration is done when multiplying the full matrix to vectors. A straightforward multiplication takes $\mathcal{O}(N^2)$ steps and is expensive. The products are instead computed in $\mathcal{O}(N)$ time using the *Fast Multipole Method*, or FMM, developed by Carrier et al. [7]. This brings the total computational time of the iterative solver down to $\mathcal{O}(N)$ from the $\mathcal{O}(N^2)$ that GMRES takes to iteratively solve full linear systems, or $\mathcal{O}(N^3)$ that a direct solver would need.

Once the solution for ω_j is found, we calculate the complex interface velocity $(u + iv)$,

$$u_j + iv_j = \sum_{i=1}^{N'} K_1'(\zeta_j, \zeta_i) w_i + i \sum_{i=1}^{N'} K_2(\zeta_j, \zeta_i)\overline{w_i} + (u_\infty + iv_\infty)_j \tag{4.3}$$

where $K_2(\zeta_j, \zeta_i)$ was defined previously and, similarly as in [10, 13],

$$K_1'(\zeta_j, \zeta_i) = -\frac{h}{2\pi}\left(\frac{[\zeta_\alpha]_i}{\zeta_i - \zeta_j} + \frac{\overline{[\zeta_\alpha]_i}}{\overline{\zeta_i - \zeta_j}}\right)$$
$$K_1'(\zeta_j, \zeta_j) = -\frac{h}{2\pi}\mathrm{Re}\left(\frac{[\zeta_{\alpha\alpha}]_j}{[\zeta_\alpha]_j}\right).$$

In vector notation, with the matrix $[K_1']$ defined from $[K_1']_{ml} = K_1'(\zeta_l, \zeta_m)$ and with $\mathcal{C}$ denoting the complex conjugation operator, the discretized velocity equation reads

$$\begin{aligned}\vec{u} + i\vec{v} &= [K_1']\vec{\omega} + i[K_2]\vec{\overline{\omega}} + (\vec{u_\infty} + i\vec{v_\infty}) \\ &= \left([K_1'] + [K_2]\mathcal{C}\right)\vec{\omega} + (\vec{u_\infty} + i\vec{v_\infty}).\end{aligned}$$

The quadrature rule used for the velocity calculation is spectrally accurate. However if only N points are used in the velocity calculations, we would start to see the growth of the modes near the Nyquist frequency when the curves become significantly deformed. These high-wavenumber instabilities are usually suppressed with high-order filters. Baker and Nachbin analyze in [5] these instabilities in the vortex sheet motion context and through a linear stability analysis show that they arise from the velocity not being adequately resolved. They further show a spectrally-accurate mid-point discretization results in a more stable method. To deal with the high-wavenumber instability, Kropinski in [13, 14] calculates the velocity at twice the number of points in physical space using an *alternating point trapezoid rule* and then truncates the spectrum to the original size. The resulting method appears to be stable, as the spectrum is effectively padded in all the velocity calculations. We employ the same quadrature, the alternating point trapezoid rule, for the velocity calculations at double the number points, but acknowledge a more thorough stability analysis is needed.

4.3 Time Integration Methods for the Interface

First we look at the interface evolution equation

$$\begin{aligned}\frac{\mathrm{d}\zeta}{\mathrm{d}t} &= -Ui\frac{\zeta_\alpha}{s_\alpha} + T\frac{\zeta_\alpha}{s_\alpha} \\ &= M(\alpha, t)\end{aligned}$$

The time integration method used to evolve the above is the Explicit Midpoint method, a two-step second order Runge-Kutta method. Denoting by n the time step so that $t^n = n\Delta t$ we have

$$\begin{aligned}\zeta^{n+\frac{1}{2}} &= \zeta^n + \frac{\Delta t}{2} M\left[\zeta^n, t^n\right] \\ \zeta^{n+1} &= \zeta^n + \Delta t M\left[\zeta^{n+\frac{1}{2}}, t^{n+\frac{1}{2}}\right].\end{aligned}$$

We emphasize that all the quantities, the interface position ζ, velocities U, S, T, angle θ, curvature $\kappa = \theta_\alpha / s_\alpha$ and so on are evaluated at time $t^{n+\frac{1}{2}} = (n+\frac{1}{2})\Delta t$ in the above process, as well as at $t^{n+1} = (n+1)\Delta t$. They will be needed in evolving in time the other quantities involved, for example arclength element s_α or the surfactant concentration Γ.

Next, we look at the arclength element s_α. Since $T_\alpha = -U\theta_\alpha + \frac{1}{2\pi}\int_0^{2\pi} U\theta_{\alpha'} d\alpha'$,

$$\begin{aligned}\frac{\mathrm{d}s_\alpha}{\mathrm{d}t} &= U\theta_\alpha + T_\alpha = \frac{1}{2\pi}\int_0^{2\pi} U\theta_{\alpha'} d\alpha' \\ &= L(\alpha, t)\end{aligned}$$

For the s_α update, we use the second-order Explicit Midpoint Runge-Kutta as well. Denoting with n the time-step, so that $t = n\Delta t$, the update is:

$$\begin{aligned}s_\alpha^{n+\frac{1}{2}} &= s_\alpha^n + \frac{\Delta t}{2} L\left[s_\alpha^n, t^n\right] \\ s_\alpha^{n+1} &= s_\alpha^n + \Delta t L\left[s_\alpha^{n+\frac{1}{2}}, t^{n+\frac{1}{2}}\right].\end{aligned}$$

The above update is written to emphasize that s_α and other interface variables are computed at time-step $n + \frac{1}{2}$. Their use will be clearer in the surfactant evolution update.

The time-integration scheme for s_α has to be fully explicit, because it is an element used in the surfactant evolution equation. However, the scheme for the interface evolution need not be; indeed an explicit-implicit approach has been often taken in similar interface problems. A *Small-Scale Decomposition* [11] of the problem can be done to identify the stiff terms in the interface evolution equation and treat them implicitly. This would lead to a less restrictive stability condition for the time step. *Implicit-Explicit*, or IMEX methods, as in [3], would then be the time-integration schemes to use, as they allow for a larger step size. This approach is taken by Kropinski for [13, 14] in the clean-flow problem. She compares the performance of fourth-order IMEX methods and that of the fourth-order Explicit Runge-Kutta methods for the interface evolution and notes that the stability requirement of the former appears similar to the Runge-Kutta method and the scheme still does not achieve the same accuracy. Thus exploit here only explicit Runge-Kutta schemes for the interface evolution. Moreover, they have added bonuses since they are self-starting and easy to use.

The Fourier spectrum of the interface is checked during the computations and if the modes near the Nyquist frequency rise above the round-off, the number of marker points N is doubled to keep the calculations well-resolved. To maintain a stable step size, the time step is then updated according to

$$\Delta t^{n+1} = \frac{1}{2}\frac{s_\alpha^{n+1}}{s_\alpha^n}\Delta t^{n+1}.$$

4.4 Time Integration Methods for the Surfactant

The time integration scheme we use for the surfactant evolution is the second-order Implicit-Explicit (IMEX) Midpoint method, a two-step Runge-Kutta scheme investigated in [4]. IMEX methods are a natural choice for these stiff convection-diffusion PDEs. One might ask why a more well-known method, like SBDF or CNAB [3], was not chosen, and the reason is the backward-differencing-formula type methods are best for equations where the diffusive part plays the most important role. In our surfactant convection-diffusion equation, especially for a large Peclet number, the surfactant dynamics is dominated mostly by the transport due to the fluid movement. Ascher et al. in [4] explain that in these cases the Implicit-Explicit Runge-Kutta methods might be a better choice, since they have a wider stability region and are self-starting. Moreover, the scheme we choose, other than having nice properties (symmetric), coincides with our choice of the integrator for the interface equations, which have to be solved simultaneously. We can thus utilize the same function evaluations and values at each step.

We explain in detail here the process of solving the surfactant equation with the IMEX Midpoint method. We can divide the convective and diffusive parts of the equation as

$$\begin{aligned}
\frac{\partial \Gamma(\alpha,t)}{\partial t} &= F(\Gamma,t) + G(\Gamma,t) \\
F(\Gamma,t) &= \frac{T}{s_\alpha}\frac{\partial \Gamma}{\partial \alpha} - \frac{1}{s_\alpha}\frac{\partial(\Gamma S)}{\partial \alpha} - \frac{1}{s_\alpha} U\Gamma \frac{\partial \theta}{\partial \alpha} \\
G(\Gamma,t) &= \frac{1}{Pe_s}\frac{1}{s_\alpha^2}\frac{\partial^2 \Gamma}{\partial \alpha^2}.
\end{aligned}$$

Taking a Discrete Fourier Transform of the surfactant partial differential equation,

$$\frac{\partial \hat{\Gamma}(k,t)}{\partial t} = \hat{F}(\Gamma,t) + \hat{G}(\Gamma,t)$$

where k denotes the wavenumber and the $\hat{F}$ and $\hat{G}$ denote the discrete Fourier transform of the functions F and G respectively.

We discretize this equation with a two-step IMEX Midpoint rule. It treats the convective part with an explicit Midpoint rule and the diffusive part with an implicit Midpoint rule.

We obtain the following updates, with n denoting the time step

$$\hat{\Gamma}^{n+\frac{1}{2}} = \hat{\Gamma}^n + \frac{\Delta t}{2}\hat{F}\left[\Gamma^n, t^n\right] + \frac{\Delta t}{2}\hat{G}\left[\Gamma^{n+\frac{1}{2}}, t^{n+\frac{1}{2}}\right]$$
$$\hat{\Gamma}^{n+1} = \hat{\Gamma}^n + \Delta t\hat{F}\left[\Gamma^{n+\frac{1}{2}}, t^{n+\frac{1}{2}}\right] + \Delta t\hat{G}\left[\Gamma^{n+1}, t^{n+1}\right].$$

We note that since $s_\alpha = s_\alpha(t)$, the Discrete Fourier transform of the diffusive part G is,

$$\hat{G}(\Gamma, t) = \frac{-k^2}{Pe_s}\frac{1}{s_\alpha^2(t)}\hat{\Gamma}(k, t),$$

hence the updates look like

$$\hat{\Gamma}^{n+\frac{1}{2}}\left(1 + \frac{\Delta t}{2}\frac{k^2}{Pe_s}\frac{1}{(s_\alpha^2)^{n+\frac{1}{2}}}\right) = \hat{\Gamma}^n + \frac{\Delta t}{2}\hat{F}\left[\Gamma^n, t^n\right]$$
$$\hat{\Gamma}^{n+1}\left(1 + \Delta t\frac{k^2}{Pe_s}\frac{1}{(s_\alpha^2)^{n+1}}\right) = \hat{\Gamma}^n + \Delta t\hat{F}\left[\Gamma^{n+\frac{1}{2}}, t^{n+\frac{1}{2}}\right],$$

from which we solve for $\hat{\Gamma}^{n+1}$ and via a Discrete Inverse Fourier Transform get Γ^{n+1}. The convective term F is found explicitly in space, then a Discrete Fourier Transform is taken to obtain $\hat{F}$ to be used in the above solver for the surfactant.

In the above surfactant update, $s_\alpha^{n+\frac{1}{2}}$, s_α^{n+1} are previously evaluated, so the arclength element needs to be updated with explicit methods. The choice time-integrating schemes for the interface and arclength element need to agree with the scheme for the surfactant .

All the methods involved in the calculations are second order; therefore, the overall method accuracy is second order. Fourth-order Runge-Kutta methods could be used in a similar way, but for our purposes second order is sufficient.

The Fourier spectrum of the surfactant variable is checked during the computations and if the modes near the Nyquist frequency rise above the round-off, the number of points N is doubled to keep the calculations well-resolved. The time step is then updated using

$$\Delta t^{n+1} = \frac{1}{2}\frac{s_\alpha^{n+1}}{s_\alpha^n}\Delta t^{n+1}.$$

Furthermore, the surfactant computation is prone to high-wavenumber instabilities because of the presence of the nonlinear terms in it involving the velocity. Again, we calculate the explicit part $F(\Gamma, t)$ at double the number of points, just as with the velocity calculation.

Chapter 5

Accuracy, Stability, Convergence

In this chapter we investigate the accuracy, stability and convergence of the algorithm and look for ways to validate our numerical scheme. The first section compares our results to the analytical solutions for a certain class of polynomial bubbles. In the second section we look at the order of convergence. The last section investigates the numerical stability of the algorithm. The algorithms here have been implemented in Fortran, the tolerance for GMRES iterations is set to 10^{-10}, and the simulations are run in a PowerMac G5 computer.

5.1 Comparisons to Analytical Solutions

Tanveer and Vanconcelos [22] exploit the complex variable theory to derive analytical solutions for a polynomial class of time-evolving bubbles in two-dimensional Stokes flow with constant surface tension. Siegel in [20, 21] and later Gilmore in [9] modify these solutions to include non-uniform surface tension and surfactant dynamics. We use their analytical solutions as a validity test for our model. Although the analytical solutions in [20] are for different polynomial bubble shapes, we concentrate here on bubble profiles that are symmetrical with respect to the x-axis and have $(N+1)$-fold symmetry.

We consider a bubble in a strain flow, undergoing no expansion/contraction; thus the area remains constant. The initial bubble shape is described by

$$z(\nu, 0) = a(0)e^{-i\nu} + b_N(0)e^{iN\nu}, \qquad \nu \in [0, 2\pi] \tag{5.1}$$

where $a(0), b_N(0)$ are real positive, and the bubble area is $A(t) = \pi[a^2(t) - Nb_N^2(t)] = A(0)$.

As argued in [22], [20], the bubble will continue to evolve according to

$$z(\nu,t) = a(t)e^{-i\nu} + b_N(t)e^{iN\nu}, \qquad \nu \in [0, 2\pi]$$

and the evolution of the parameters $a(t), b_N(t)$ are found [20] through

$$\frac{\mathrm{d}(ab_N)}{\mathrm{d}t} = -(N+1)ab_N I_0(a,b_N) + Qa^2\delta_{N+2,3}, \tag{5.2}$$

and for the varying surface tension $\sigma(\nu,t) = 1 - \beta\Gamma(\nu,t)$ we have

$$I_0(a,b_N) = \frac{1}{4\pi}\int_0^{2\pi} \frac{\sigma(\nu',t)}{|z_{\nu'}(\nu',t)|}d\nu' = \frac{1}{4\pi}\int_0^{2\pi} \frac{1}{|z_{\nu'}(\nu',t)|}d\nu' - \frac{\beta}{4\pi}\int_0^{2\pi} \frac{\Gamma(\nu',t)}{|z_{\nu'}(\nu',t)|}d\nu' \tag{5.3}$$

The second integral in (5.3) vanishes because

$$\begin{aligned}\int_0^{2\pi} \frac{\Gamma(\nu')}{|z_{\nu'}(\nu')|}d\nu' &= \frac{1}{|z_{\nu'}(\nu')|^2}\Big|_0^{2\pi}\int_0^{2\pi}\Gamma(\nu')|z_{\nu'}(\nu')|d\nu' + \int_0^{2\pi}\Gamma_\nu(\nu')d\nu' \\ &= \left(|z_{\nu'}(2\pi)|^{-2} - |z_{\nu'}(0)|^{-2}\right)(2\pi) + (\Gamma(2\pi) - \Gamma(0)) \quad = 0\end{aligned}$$

where we have also used the insolubility of surfactant, $\int_0^{2\pi}\Gamma(\nu')|z_{\nu'}(\nu')|d\nu' = 2\pi$.

Using (5.1) we see that $|z_{\nu'}(\nu',t)| = [a^2 + N^2b_N^2 - 2Nab_N\cos(2\nu')]^{1/2}$, and for (5.3) we obtain, similar to [13] and [9],

$$\begin{aligned}I_0(a,b_N) &= \frac{1}{4\pi}\int_0^{2\pi}\frac{1}{[a^2+N^2b_N^2-2Nab_N\cos(2\nu')]^{1/2}}d\nu' \\ &= \frac{1}{\pi|a|}\frac{a}{a+b_N}K\left[\frac{4ab_N}{(a+b_N)^2}\right],\end{aligned}$$

and K is a complete elliptic integral of the first kind [1], defined by

$$K(f) = \int_0^{\pi/2}(1 - f\sin^2(\nu))^{-1/2}d\nu.$$

Of course the above computes only the interface evolution. In this frame of reference, the surfactant will evolve according to the following equation, as found in [20], [9]:

$$\frac{\partial\Gamma}{\partial t} = \mathrm{Re}\left(\frac{\mathrm{d}z}{\mathrm{d}t}\frac{\Gamma_\nu}{z_\nu}\right) - \frac{1}{|z_\nu|}\frac{\partial}{\partial\nu}\mathrm{Re}(P) + \frac{1}{|z_\nu|}\mathrm{Im}(\frac{z_{\nu\nu}}{z_\nu})\mathrm{Im}(P) + \frac{1}{Pe_s|z_\nu|}\frac{\partial}{\partial\nu}\left(\frac{\Gamma_\nu}{|z_\nu|}\right), \tag{5.4}$$

where

$$
\begin{aligned}
P(\nu,t) &= \frac{\mathbf{u}}{|z_\nu|}\bar{z}_\nu\Gamma \\
\frac{\mathrm{d}z}{\mathrm{d}t} &= \frac{\mathrm{d}a}{\mathrm{d}t}e^{-i\nu} + \frac{\mathrm{d}b_N}{\mathrm{d}t}e^{iN\nu} \\
\mathbf{u} &= \frac{\mathrm{d}z}{\mathrm{d}t} - z_\nu e^{2i\nu}\left[\frac{1}{4\pi}PV\int_0^{2\pi}\frac{\sigma(\nu',t)}{|z_\nu(\nu',t)|}\cot\left(\frac{\nu'-\nu}{2}\right)d\nu'\right], \\
&= \frac{\mathrm{d}z}{\mathrm{d}t} - z_\nu e^{2i\nu}\left[-\frac{1}{2i}\mathcal{H}\left(\frac{\sigma}{|z_\nu|}\right)\right].
\end{aligned}
$$

Here $\mathcal{H}$ is the Hilbert transform, a skew-symmetric linear operator, diagonalizable by the Fourier Transform, hence effectively computed in Fourier space using

$$\mathcal{H}(e^{ikx}) = -i\ \mathrm{sign}(k)e^{ikx}, \quad \mathcal{H}(1) = 0.$$

The analytical solutions for the surfactant-laden bubble interface now consist of solving the equations (5.2) and (5.4) given initial bubble and surfactant profiles, as well as the parameters defining the flow and surfactant evolution, β, Q and Pe_s.

The simplest case to check is that of an initially circular bubble profile with radius 1. In this case the parameters are $N = 1$, $a(0) = 1$ and $b_N(0) = b(0) = 0$, and the equations defining problem become

$$
\begin{aligned}
\frac{\mathrm{d}(ab)}{\mathrm{d}t} &= -2abI_0(a,b) + Qa^2 \\
a^2 - b^2 &= 1 \\
I_0(a,b) &= \frac{1}{\pi|a|}\frac{a}{a+b}K\left[\frac{4ab}{(a+b)^2}\right] \\
\frac{\partial\Gamma}{\partial t} &= \mathrm{Re}\left(\frac{\mathrm{d}z}{\mathrm{d}t}\frac{\Gamma_\nu}{z_\nu}\right) - \frac{1}{|z_\nu|}\frac{\partial}{\partial\nu}\mathrm{Re}(P) + \frac{1}{|z_\nu|}\mathrm{Im}(\frac{z_{\nu\nu}}{z_\nu})\mathrm{Im}(P) + \frac{1}{Pe_s|z_\nu|}\frac{\partial}{\partial\nu}\left(\frac{\Gamma_\nu}{|z_\nu|}\right).
\end{aligned}
$$

We integrate this system of equations using a fourth order Explicit Runge-Kutta method to achieve the highest accuracy we can afford in the analytical solutions $z(\nu,t)$ and $\Gamma(\nu,t)$.

To compare with our numerical model, in which the interface $\zeta(\alpha,t)$ has equi-arclength spacing, we have to equi-parametrize the analytical solution $z(\nu,t)$ for the interface and get $z(\alpha',t)$. This is achieved by following the procedure outlined in [11]. Next we use *Fourier Interpolation* to find the surfactant values $\Gamma(\alpha',t)$ from the values $\Gamma(\nu,t)$.

For the following comparison the parameters are $\beta = 0.1$, $Q = 0.15$, $Pe_s = 10^3$, the spatial mesh has $N = 128$ points and and the time-step is $\Delta t = 0.001$. (For the analytical solutions, the integrating method is explicit, so we need $\Delta t = \mathcal{O}(1/N^2)$). We compare the bubble profiles $z(\alpha', t)$ and $z(\alpha, t)$ and plot the difference in Fig. 5.1, and do the same for the analytical surfactant solution $\Gamma(\alpha', t)$ and our numerical solution $\Gamma(\alpha, t)$ in Fig. 5.2.

According to the analysis in [20], for these parameters, the bubble will evolve to a steady-state, and so will the surfactant concentration Γ. The flow advects the surfactant toward the bubble tips, where it accumulates and eventually forms *surfactant caps*, or areas of non-zero concentration, whereas the other interface parts are left devoid of surfactant.

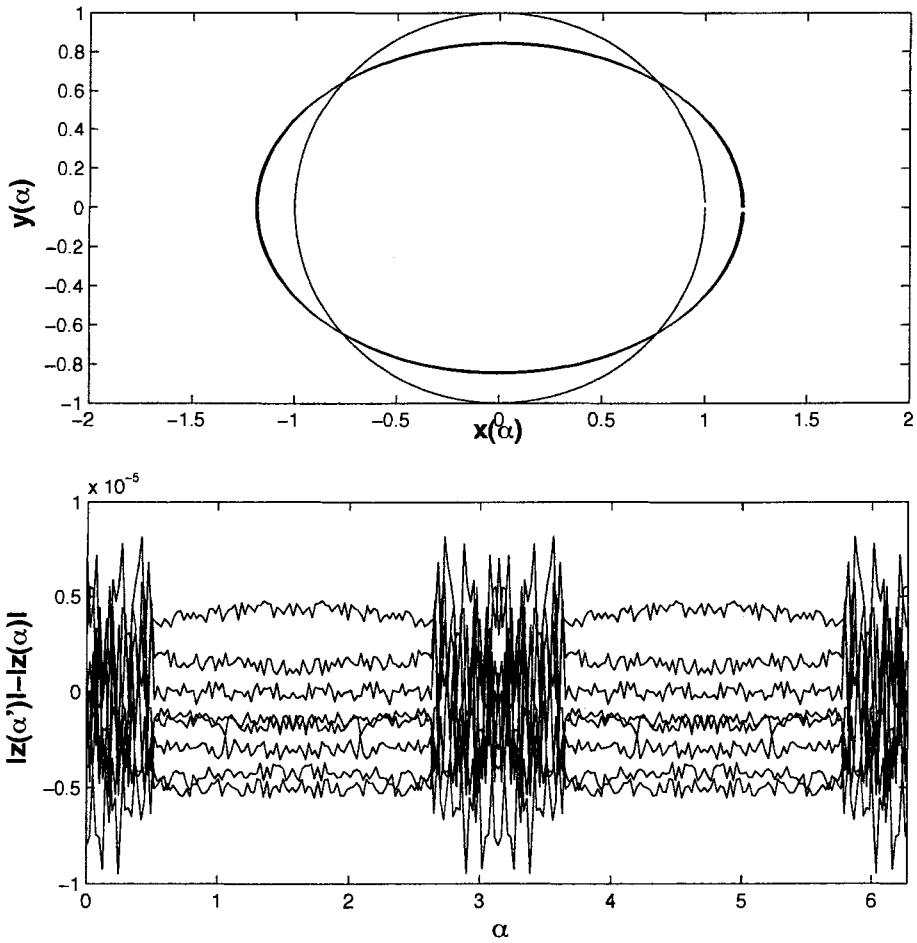

Figure 5.1: *Comparison with the analytical solution: the bubble profiles for the analytical solution $z(\alpha')$ and the numerical solution $z(\alpha)$. The second plot shows their differences.*

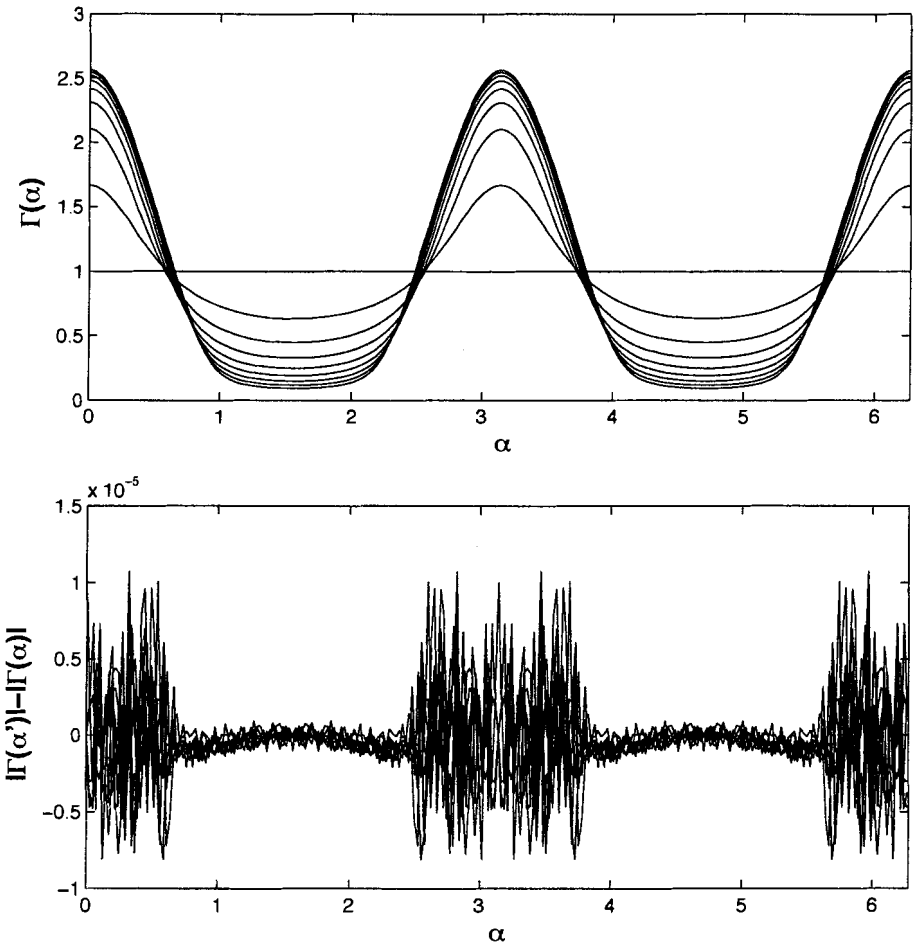

Figure 5.2: *Comparison with the analytical solution: the surfactant profiles for the analytical solution* $\Gamma(\alpha')$ *and the numerical solution* $\Gamma(\alpha)$. *The second plot shows their differences.*

We notice that both for the bubble interface $z(\alpha)$ and for the surfactant $\Gamma(\alpha)$ the relative error to the analytical solution is $\mathcal{O}(10^{-6})$, or $\mathcal{O}((\Delta t)^2)$. This can be seen in table 5.1, where we write the results for $||z(\alpha') - z(\alpha)||_\infty$ and $||\Gamma(\alpha') - \Gamma(\alpha)||_\infty$, or the maximum errors between the solutions.

The area of the bubble in the analytical solutions, namely

$$A(t) = \pi[a(t)^2 - Nb_N(t)^2]$$

can also be compared to the numerically computed bubble area in our solutions. Another

Table 5.1: *Comparison with the analytical solution: the errors at time T=0,4,8,...,32.*

	$T=4$	$T=8$	$T=12$	$T=16$
$\|\|z(\alpha')-z(\alpha)\|\|_\infty$	8.1752×10^{-6}	4.7945×10^{-6}	5.7361×10^{-6}	4.5497×10^{-6}
$\|\|\Gamma(\alpha')-\Gamma(\alpha)\|\|_\infty$	1.0000×10^{-5}	7.4219×10^{-6}	7.3334×10^{-6}	1.0051×10^{-5}
	$T=20$	$T=24$	$T=28$	$T=32$
$\|\|z(\alpha')-z(\alpha)\|\|_\infty$	9.2326×10^{-6}	4.8201×10^{-6}	9.4566×10^{-6}	6.8305×10^{-6}
$\|\|\Gamma(\alpha')-\Gamma(\alpha)\|\|_\infty$	8.0755×10^{-6}	1.0723×10^{-5}	9.6307×10^{-6}	6.9850×10^{-6}

variable whose value we can predict for the analytical solutions is the maximum curvature κ_{max}, as shown in [13], computed according to

$$\kappa_{max} = \frac{a(t) + b_N(t)N^2}{(a(t) - b_N(t)N)^2},$$

so we use this information to compare the accuracy of the curvature in the numerical calculations as well. Table 5.2 shows the errors in $|z(\alpha)|$, $\Gamma(\alpha)$, area A and maximum curvature κ_{max} for a few different initial time steps Δt_0.

The simulations are run for the same parameters as in the previous example, namely $\beta = 0.1$, $Q = 0.15$, $Pe_s = 10^3$, up to time $T = 1$. Comparisons are made to the analytical solutions which are computed using an explicit Runge-Kutta method of order four.

Table 5.2: *Comparison with the analytical solution: the errors for different* Δt.

Δt_0	Error in $\|z(\alpha)\|$	Error in $\Gamma(\alpha)$	Error in A	Error in κ_{max}
0.001	7.02567×10^{-6}	6.00921×10^{-6}	1.74881×10^{-7}	9.01516×10^{-7}
0.0005	9.00000×10^{-7}	9.21277×10^{-7}	4.37092×10^{-8}	1.13516×10^{-7}
0.00025	2.11794×10^{-8}	4.57183×10^{-8}	1.09210×10^{-9}	5.27671×10^{-8}
0.000125	8.33482×10^{-9}	4.00948×10^{-9}	2.73145×10^{-10}	6.32970×10^{-9}

Similar comparisons for cases with different parameters β, Q, Pe_s can be shown, but they all confirm what we see in this example: our numerical solutions are convergent and accurate to $\mathcal{O}((\Delta t)^2)$ for this polynomial class of bubbles. This comparison with the analytical solutions validates our model. We can go further to infer that numerical solutions for non-polynomial bubble profiles are going to be convergent and second order accurate as well.

5.2 The Order of Temporal Convergence

We can check the numerical accuracy of the calculations in several ways. The easiest two ways are to check the area of the bubble and the total amount of surfactant on the bubble. They should remain constant in time, the first because we assumed the bubble is non-shrinking and non-expanding and the later because we assumed the surfactant is insoluble.

We verify the accuracy of our surfactant calculations by checking the error in the total amount of surfactant. The total should remain fixed, i.e. the surfactant flux into the outside fluid is zero. However when numerically computing the values, we expect the accuracy of the numerical integration schemes to be reflected in the surfactant total difference $\Delta(\Gamma \text{ Total})$, because

$$0 = \Delta(\Gamma \text{ Total}) = \frac{d}{dt}\int_0^{2\pi} \Gamma(\alpha', t) s_\alpha(t) d\alpha'$$

and Γ and s_α are $\mathcal{O}((\Delta t)^2)$ accurate. Thus we expect the difference in the total amount of surfactant to be $\mathcal{O}((\Delta t)^2)$.

FourierIntegration is used to compute the integrals involved in the flux, and we calculate the difference between the surfactant total values at time-steps n and $n+1$

$$\Delta(\Gamma \text{ Total})^n = \left[\int_0^{2\pi} \Gamma(\alpha', t) s_{\alpha'}(t) d\alpha'\right]^{n+1} - \left[\int_0^{2\pi} \Gamma(\alpha', t) s_{\alpha'}(t) d\alpha'\right]^{n}.$$

Similarly for the bubble area, the error in time should be zero. The area difference ΔA in each time-step is

$$\Delta \mathrm{A}^n = A^{n+1} - A^n.$$

Figure 5.3 shows how the surfactant total and the bubble area are changing in time. Figure 5.4 shows how the numerical surfactant flux and the area are changing with respect to Δt for a simulation with the same parameters used in the previous section at the final time $T = 1$. In the same figure we have plotted the error in the interface $\zeta(\alpha)$, the error in the surfactant $\Gamma(\alpha)$, the error in the area A and the error in the maximum curvature κ_{max} at time $T = 1$, because, as we discussed in the previous section, we can check these values for the flow parameters used in the simulation.

From figure 5.4 we can now infer that the overall accuracy of the solutions is $\mathcal{O}((\Delta t)^2)$.

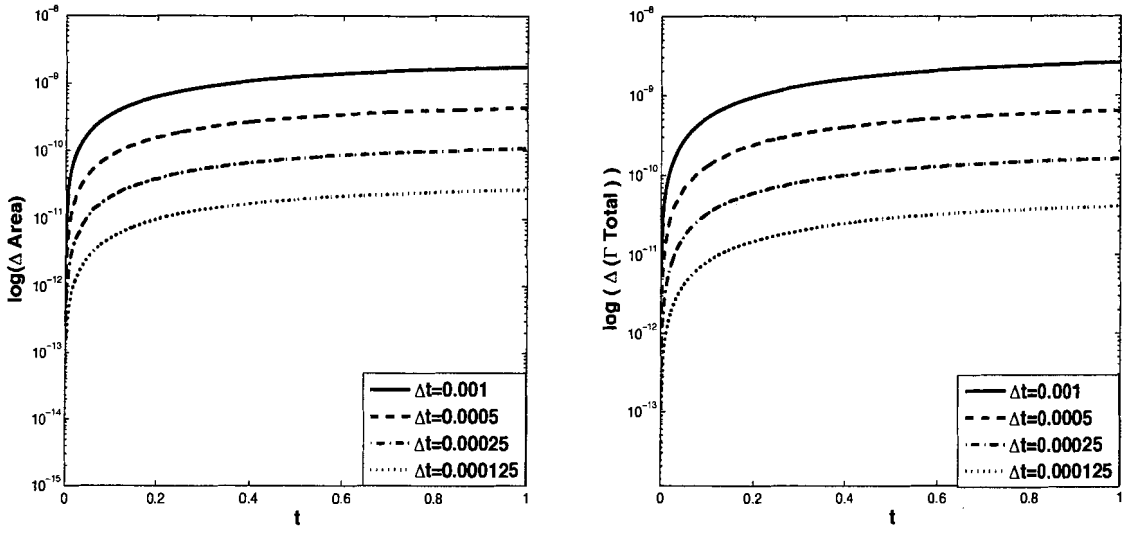

Figure 5.3: *The errors in the bubble area (left) and surfactant total (right) for four different time-steps. Notice that the errors do not fall much below* $\mathcal{O}(10^{-10})$*, the tolerance set for the GMRES iterations. The errors start to level at* $\mathcal{O}((\Delta t)^2)$ *for each of the* Δt*-s here, and that is the numerical scheme's accuracy.*

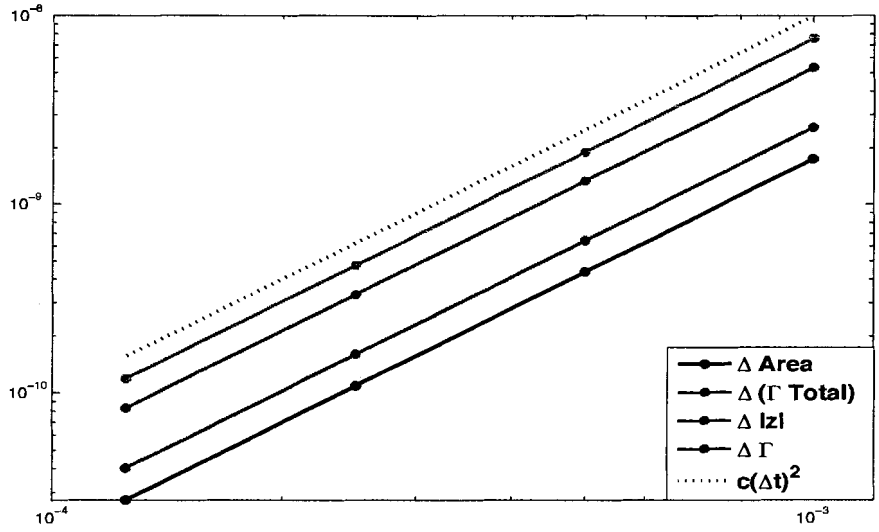

Figure 5.4: *The numerical accuracy in the calculation of the bubble area, total amount of surfactant, interface position and surfactant concentration. We notice from the errors' slopes, which are all two as seen in the comparison with the* $c(\Delta t)^2$ *line, that second order convergence is achieved in the computations.*

5.3 The Numerical Stability of the Schemes

We mentioned in the previous chapter that the velocity needs to be calculated in double the number of points to suppress the high-wavenumber instabilities that would usually arise in such computations. We do the same with the explicit part of the surfactant equation, since the presence of the velocity terms there is suspected to cause high-wavenumber instabilities in the surfactant evolution. These can be seen in the figure 5.5 from the surfactant variable's Fourier Transforms for an unpadded and a padded simulation of a time-evolving bubble.

We investigate the stability of the scheme by checking the eigenvalues of the Jacobian matrix of the interface equation and surfactant equation (3.8)

$$\frac{\mathrm{d}\zeta}{\mathrm{d}t} = -Ui\frac{\zeta_\alpha}{s_\alpha} + T\frac{\zeta_\alpha}{s_\alpha} \equiv \mathcal{F}^\zeta(\zeta, t)$$
$$\frac{\partial\Gamma}{\partial t} = \frac{T}{s_\alpha}\frac{\partial\Gamma}{\partial\alpha} - \frac{1}{s_\alpha}\frac{\partial(\Gamma S)}{\partial\alpha} - \frac{1}{s_\alpha}U\Gamma\frac{\partial\theta}{\partial\alpha} + \frac{1}{Pe_s}\frac{1}{s_\alpha^2}\frac{\partial^2\Gamma}{\partial\alpha^2} \equiv \mathcal{F}^\Gamma(\Gamma, t).$$

The entries of the $(N \times N)$ Jacobian matrices are calculated as follows:

$$\mathcal{J}^\zeta_{ij} = \frac{\mathcal{F}^\zeta_j(\zeta_i + \Delta, t) - \mathcal{F}^\zeta_j(\zeta_i, t)}{\Delta} \qquad i, j = 1, ..., N$$
$$\mathcal{J}^\Gamma_{ij} = \frac{\mathcal{F}^\Gamma_j(\Gamma_i + \Delta, t) - \mathcal{F}^\Gamma_j(\Gamma_i, t)}{\Delta} \qquad i, j = 1, ..., N$$

where Δ is a "sufficiently small" number, which for our purposes we take to be 10^{-6}. The eigenvalues of the Jacobian matrices $\mathcal{J}^\zeta$ and $\mathcal{J}^\Gamma$ are then computed and plotted.

In figures 5.6 - 5.8 we show the pseudo-eigenspectra of $\mathcal{J}^\zeta$ and $\mathcal{J}^\Gamma$ for an initially circular bubble expanding in a flow with parameters $Q = 0.02$, $Pe_s = 10^3$, $\beta = 0.1$ at time $T = 0.5$. The eigenspectra plots look similar for computations with other stable flow parameters.

From the plots, we notice that the unpadded computations appear unstable, whereas the padded ones are stable. As N increases, we see an appearance of the real positive eigenvalues in the unpadded interface and surfactant computations. These eigenvalues' magnitudes grow with increasing N. The eigenspectrum plot of the interface in Fig. 5.6 is truncated and the largest negative eigenvalues are not shown, but they increase linearly in N, suggesting a stable time-step of $\mathcal{O}(1/N)$. This is more clear with the surfactant spectrum in Fig.5.7, since we have rescaled the plots to make evident that the eigenvalue magnitudes grow linearly with N. This confirms a stable time-step size of $\mathcal{O}(1/N)$ for the surfactant calculation.

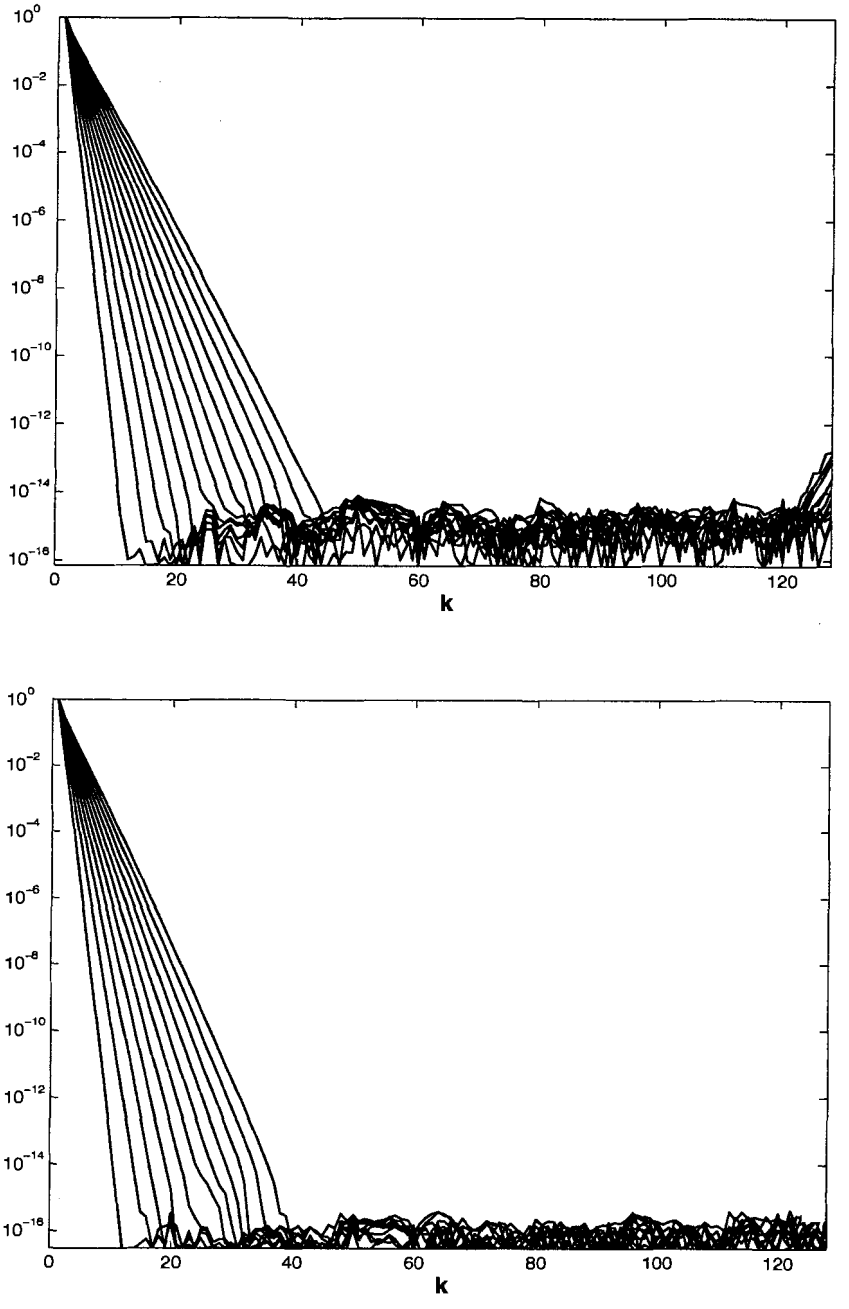

Figure 5.5: *The Fourier transforms* $\log(\hat{\Gamma}_k)$ *of the evolution of an initially circular bubble with parameters* $Q = 0.51$, $Pe_s = 10^3$, $\beta = 0.1$ *at times 0:0.5:1 in an unpadded (top) and padded (bottom) computation. The upper plot shows high-wavenumber instabilities arising, while the bottom plot shows a simulation where the surfactant variable* Γ *is well-resolved.*

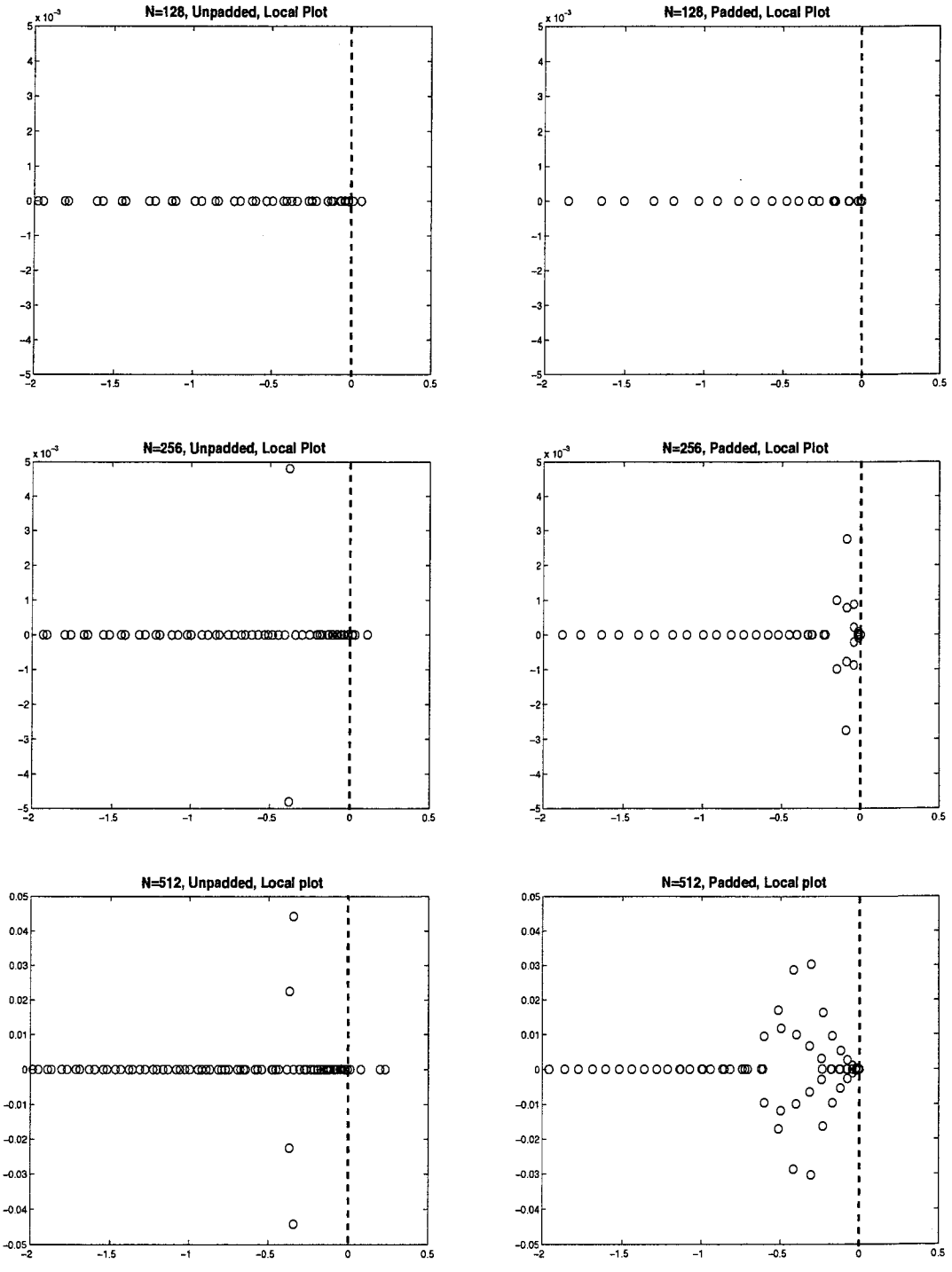

Figure 5.6: *The instantaneous eigenvalues of the Jacobian Matrix for the interface* ζ.

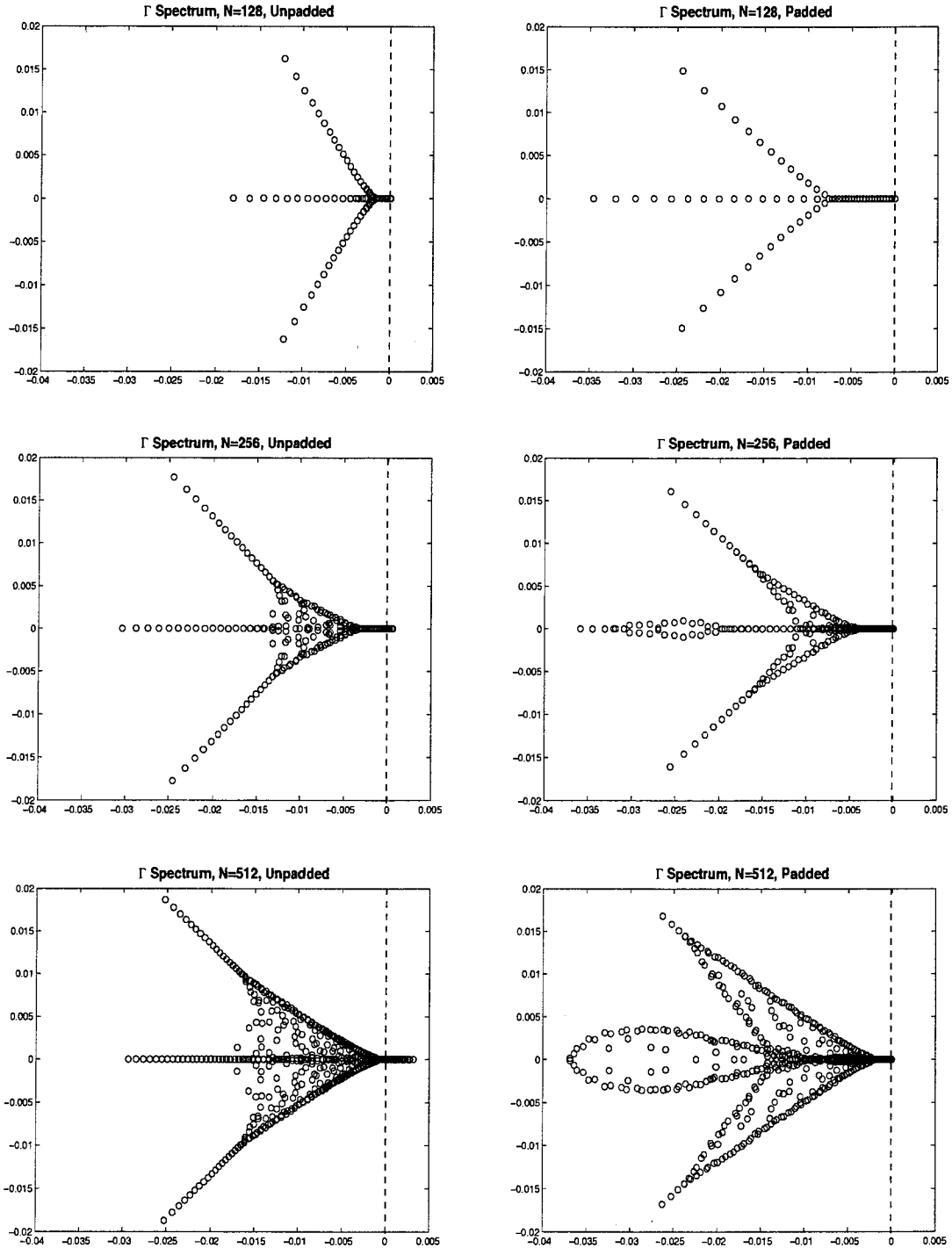

Figure 5.7: *The instantaneous eigenvalues of the Jacobian Matrix for the surfactant* Γ*, scaled by 1/128, 1/256 and 1/512 respectively to display the full spectrum and the modes linear growth.*

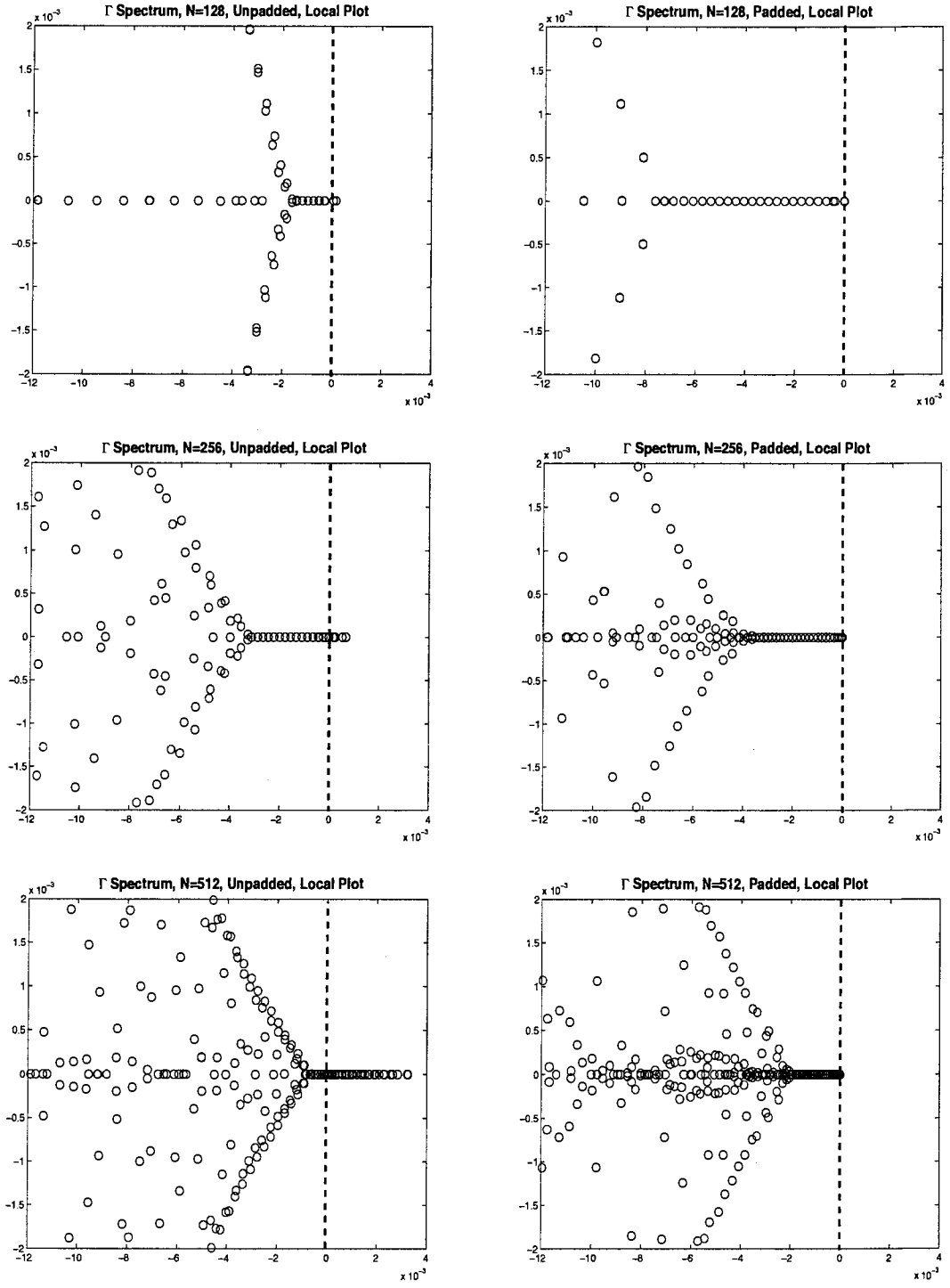

Figure 5.8: *Local plot of the instantaneous eigenvalues of the Jacobian Matrix for the surfactant* Γ *scaled by 1/128, 1/256 and 1/512 respectively for comparison.*

Chapter 6

Various Numerical Investigations

In this section we present a few numerical calculations to show what our numerical model is capable of doing, as well as look into the various physical phenomena that occur when surfactants are present on the bubble interface. The first case looks at the formation of surfactant caps. Section two compares the surfactant-laden interfaces to the clean interfaces. The third investigation aims to show how surfactant affects the bubble shapes in high Capillary number flows, and in particular how it affects bubble breakups. The last section looks at the deformation of bubbles with a non-uniform initial surfactant layer.

6.1 Surfactant Caps on Bubbles

Siegel in [20] provides a detailed analysis to determine the parameters β, Pe_s and Q for which the bubble interface is stable, reaches a steady state, and so does the surfactant concentration. Moreover, he provides an analysis to show for which parameters the surfactant caps are formed. Caps are the areas on the bubble where there is non-zero surfactant layer, when the rest are bare of it. In this section we look at a few cases of terminal surfactant shapes for various parameters, in particular surfactant caps.

The first plot in Fig. 6.1 shows the settling of the bubble interface and surfactant concentration for $\beta = 0.1$, $Pe_s = 10^3$ and $Q = 0.15$. The second figure looks at the surfactant caps occurrences when Q is doubled. Here the caps are more obvious. The last example in Fig.6.1 is with Q beyond the critical Capillary number for surfactant cap formation ($Q = 0.40$ for this β and Pe_s from [20]), although for these examples steadying of the interface and surfactant profiles still happen.

6.2 Comparisons for Diminishing Surfactant Influence

A question many may ask is "How do the surfactants affect the bubble interface profile and how does the surfactant-laden flow differ from the clean flow?". We address this question in this section, by comparing the bubble interface and surfactant profiles for diminishing surfactant effects, i.e. for $\beta = 0.1, 0.05, 0.025$ and $\beta = 0$, the clean flow case.

We run tests with Capillary number $Q = 0.41$, Peclet number $Pe_s = 10^3$ for an initially circular bubble with $\Gamma(\alpha, 0) = 1$. The bubble is expected to remain elliptical in shape throughout its time-evolution [20]. We introduce the deformation parameter D

$$D = \frac{R_{max} - R_{min}}{R_{max} + R_{min}}$$

where R_{max} and R_{min} are the maximum and minimum radial distances of an interface point from the bubble center. We compare D, the maximum and minimum of the surfactant and the surface tension on the interface for the various cases in tables 6.1 and 6.2.

Table 6.1: *Comparisons of diminishing surfactant effects on the bubble interface at $T = 2$.*

	R_{max}	R_{min}	D	Γ_{max}	Γ_{min}	σ_{max}	σ_{min}
$\beta = 0.100$	1.6439	0.6083	0.4598	3.8613	0.3303	0.9670	0.6139
$\beta = 0.050$	1.5914	0.6284	0.4338	5.0927	0.3149	0.9843	0.7454
$\beta = 0.025$	1.5662	0.6385	0.4208	6.4294	0.3069	0.9923	0.8393
$\beta = 0.000$	1.5419	0.6484	0.4079	0.0000	0.0000	1.0000	1.0000

Table 6.2: *Comparisons of diminishing surfactant effects on the bubble interface at $T = 7$.*

	R_{max}	R_{min}	D	Γ_{max}	Γ_{min}	σ_{max}	σ_{min}
$\beta = 0.100$	1.7769	0.5628	0.5189	5.0339	0.1812	0.9819	0.4966
$\beta = 0.050$	1.6725	0.5979	0.4733	7.1477	0.1616	0.9919	0.6426
$\beta = 0.025$	1.6246	0.6155	0.4505	9.8252	0.1516	0.9962	0.7544
$\beta = 0.000$	1.5744	0.6352	0.4251	0.0000	0.0000	1.0000	1.0000

With diminishing surfactant effects (diminishing β), the bubble deforms less and the results approach those of the clean flow, $\beta = 0.0$. The surfactant accumulation at the bubble tips lowers the surface tension and increases motility in those areas, as seen in figure 6.2. This can be seen from the tables 6.1, 6.2 and plots in figure 6.2, where for higher surfactant effects (increasing β) the bubble deformation tends to be higher, for the same flow strain (specified by Q) and the surfactant diffusion (specified by Pe_s).

Notice in figure 6.2 how the interface dynamics has in turn affected the time-evolution for the surfactant concentration: for lower β the surfactant evolution is more advanced. One reason is that the interface is moving slower and thus the normal velocity U is smaller. The bubble is less deformed, so the curvature κ is also smaller. The term $(-\Gamma U\kappa)$ in the surfactant equation (3.8) is bigger, hence $d\Gamma/dt$ is bigger and Γ increases faster.

6.3 Surfactant and Bubble Breakup

Some analysis is done to determine the parameters β, Pe_s and Q for which the bubble interface is stable and reaches a steady state, and for which it is unstable and continues to evolve and stretch indefinitely [6, 16, 21] . This is known in literature as bubble bursting. It is widely believed that the surfactant layer on the interface affects the breakup state.

Figure 6.3 shows bubbles fracturing for a large strain $Q = 0.80$ and large diffusivity $Pe_s = 10$ at time $T = 7$. The figure shows the cases with $\beta = 0.2$, $\beta = 0.1$ and $\beta = 0.0$, the clean flow. The presence of surfactants in the "bubble belt" (see figure 6.4), has lowered the surface tension there, increased motility and thus is facilitating the bubble pinching.

The linear equation of state has its drawbacks, e.g. numerical negative surface tension artefacts, so other equations of state need to be considered. This is future work.

6.4 Bubbles and Non-Uniform Surfactant

For completeness, we present the evolution of bubbles with initially non-uniform surfactant layers on them and see how the interface motility is affected.

The first example in figure 6.5 shows the evolution of an initially-circular bubble with surfactant profile $\Gamma(\alpha, 0) = 1 + \cos(\alpha)/2$ to time $T = 7$. We can see that the surfactant distribution has affected the bubble evolution: its position is no longer symmetric about the y-axis. This is an occurrence that our model is able to accurately simulate, while the analytical solutions of Siegel [20, 9] cannot quite capture this, given the imposed symmetry on the interface from the parameters a and b_N (refer to the equations in section 5.1).

The evolution of an initially-circular bubble with initial surfactant profile $\Gamma(\alpha, 0) = 1 + \sin(\alpha)/2$ in figure 6.5 shows the bubble has a terminal position which is not symmetric about the x-axis. This happens because of the non-uniformity in the surfactant, hence non-uniformity in the surface tension. The parameters used are $Q = 0.15$, $\beta = 0.1$, $Pe_s = 10^3$.

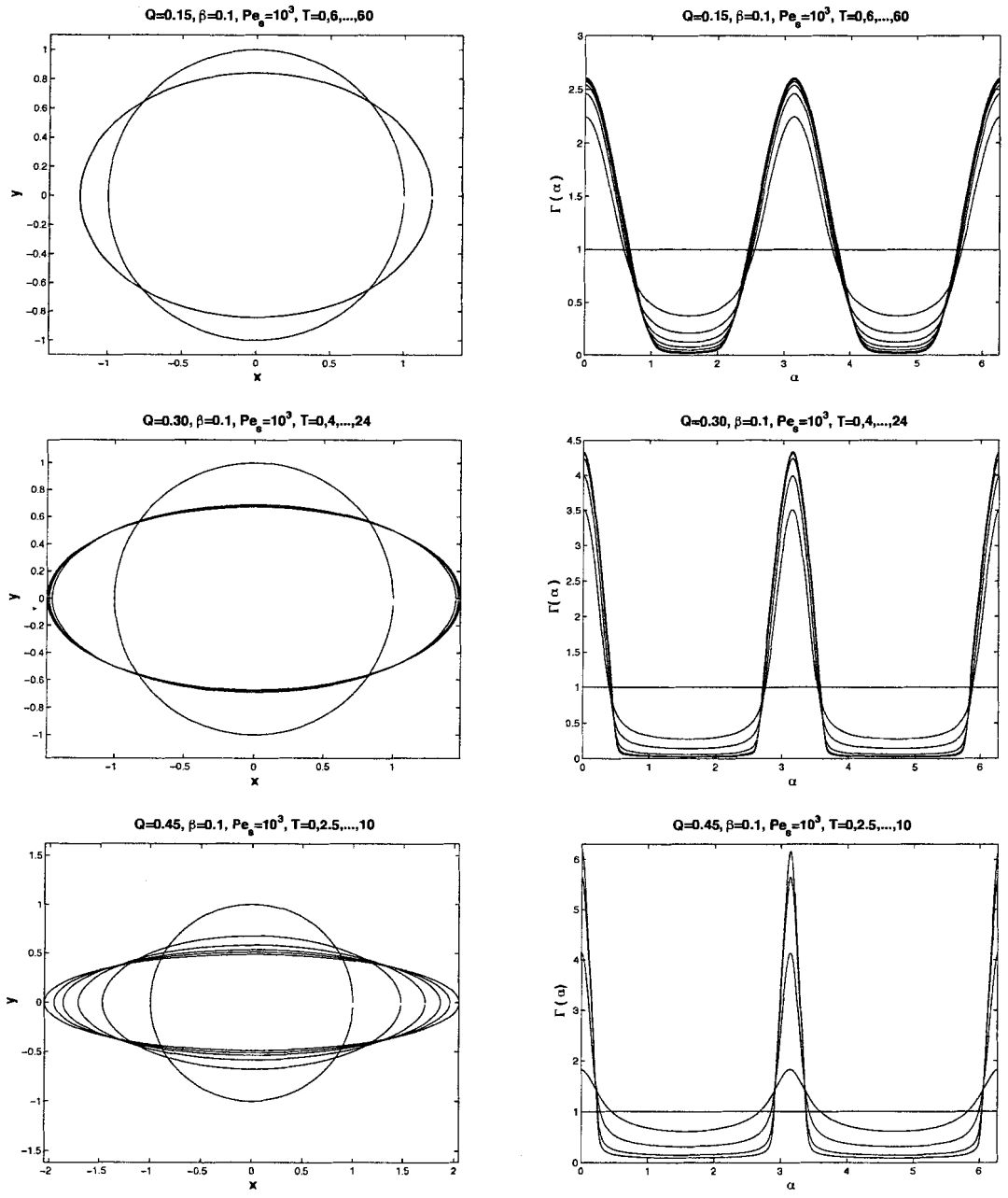

Figure 6.1: *Surfactant cap occurrences for* $\beta = 0.1$, $Pe_s = 10^3$. *The first two examples, with* $Q = 0.15$ *and* $Q = 0.30$ *respectively, are cases when surfactant caps form. The last example, with* $Q = 0.45$ *is beyond the threshold for surfactant cap formation.*

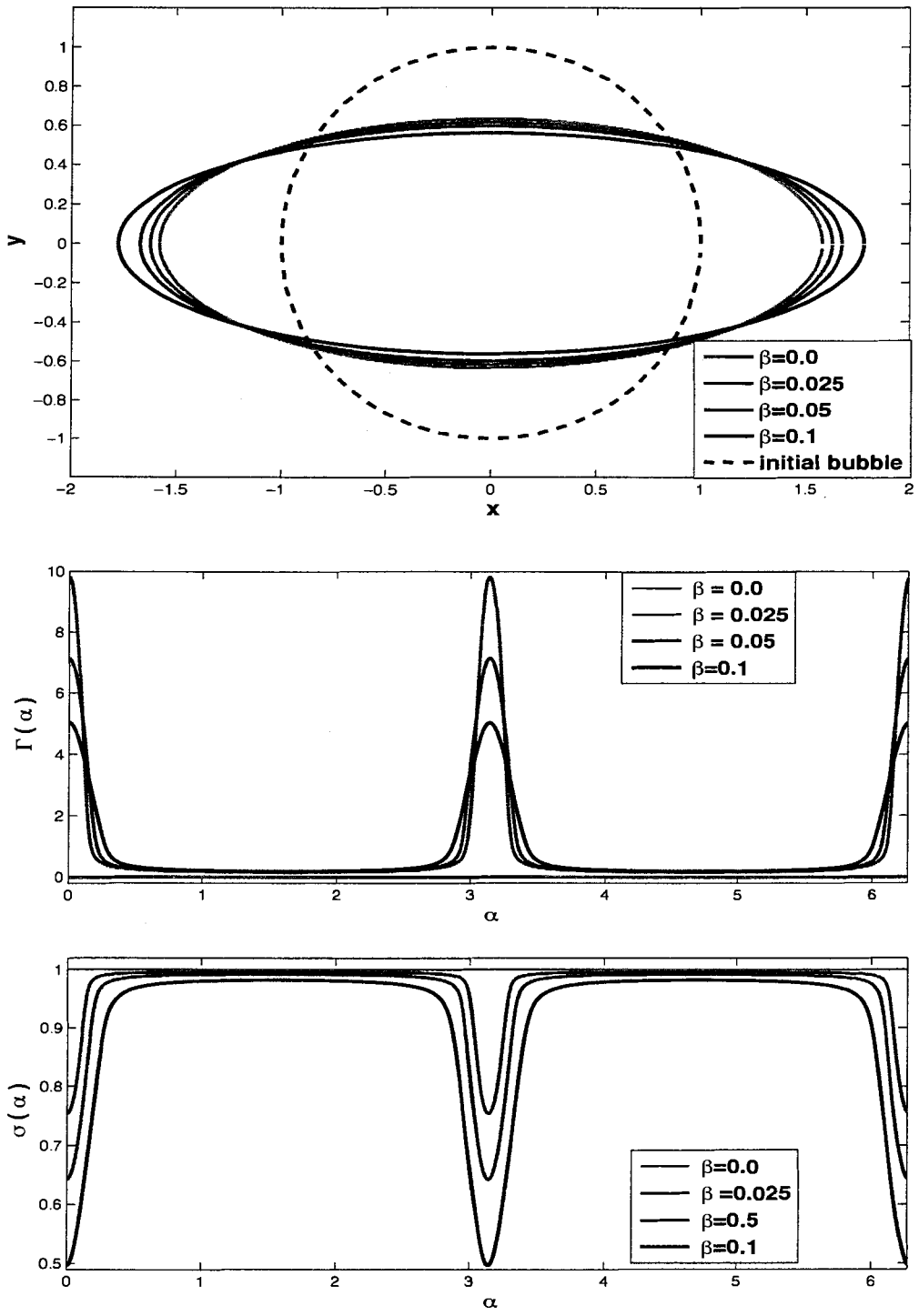

Figure 6.2: *Superimposed plots of the interface (top), surfactant (middle) and surface tension (last) profiles at $T = 7$ for diminishing β values.*

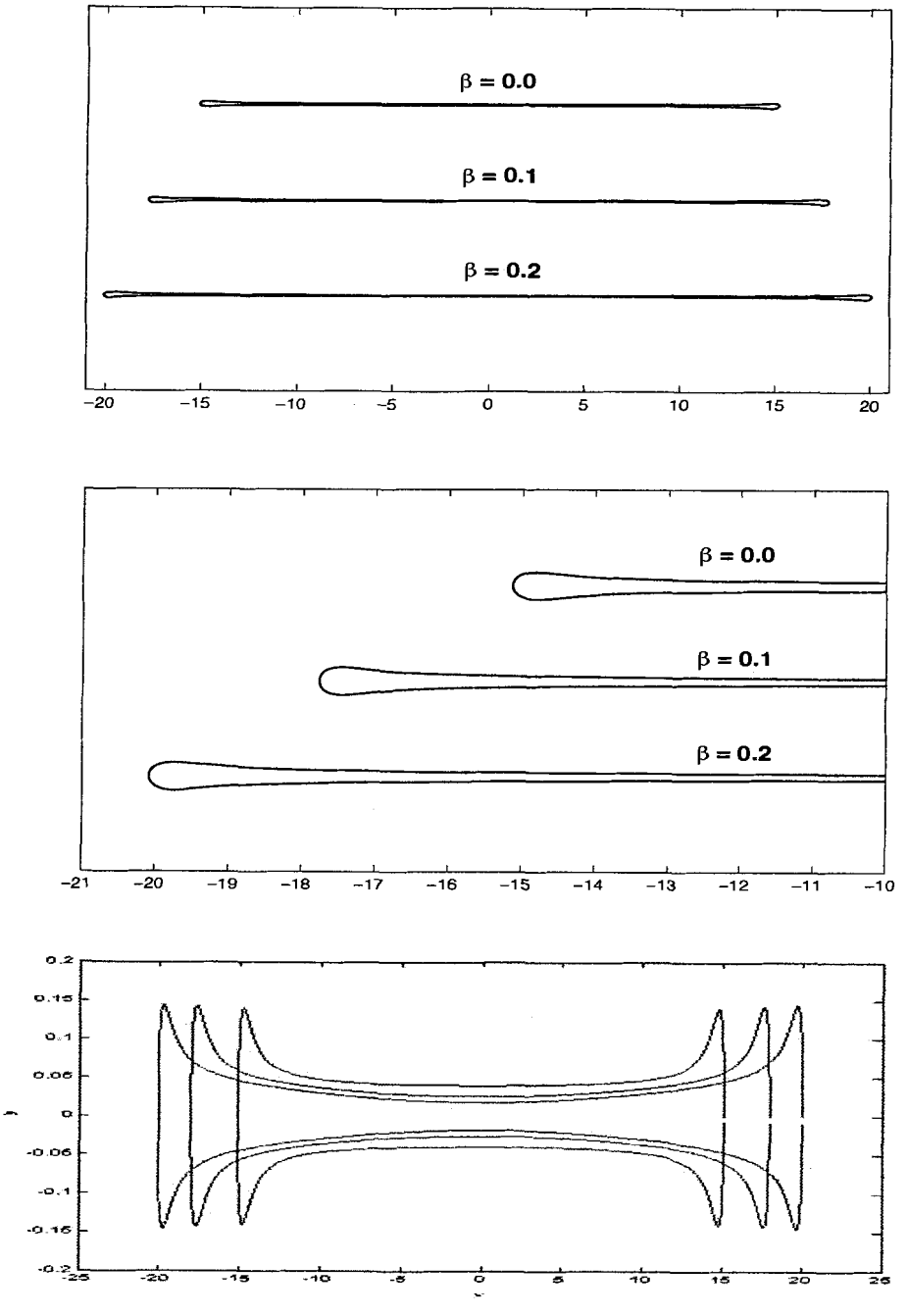

Figure 6.3: *Bursting bubble profiles at time* $T = 7$ *for parameters* $Q = 0.40$, $Pe_s = 10$ *and different surfactant influence* $\beta = 0.0, 0.1$ *and* 0.2. *The third plot is horizontally compressed to show the bubble neck widths, as the the bubbles are very stretched. In the third plot, the (horizontally) outermost profile is* $\beta = 0.2$, *the middle profile is* $\beta = 0.1$ *and the (horizontally) innermost profile is* $\beta = 0.0$, *the clean flow.*

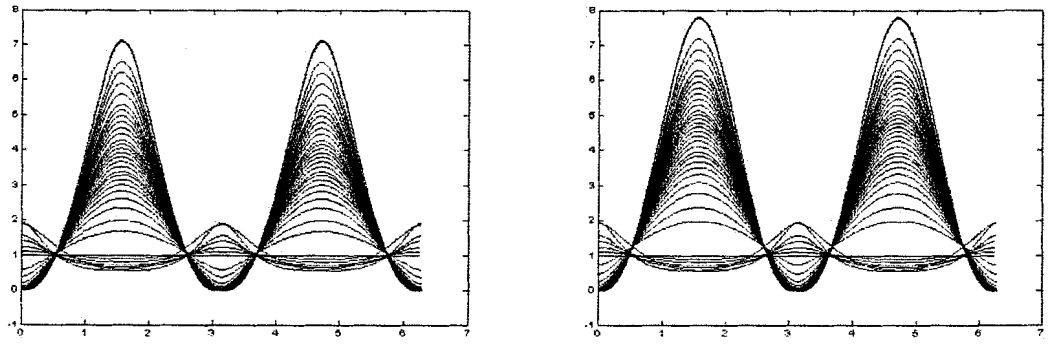

Figure 6.4: *Bubble bursting, the surfactant profiles for* $\beta = 0.2$ *and* $\beta = 0.1$.

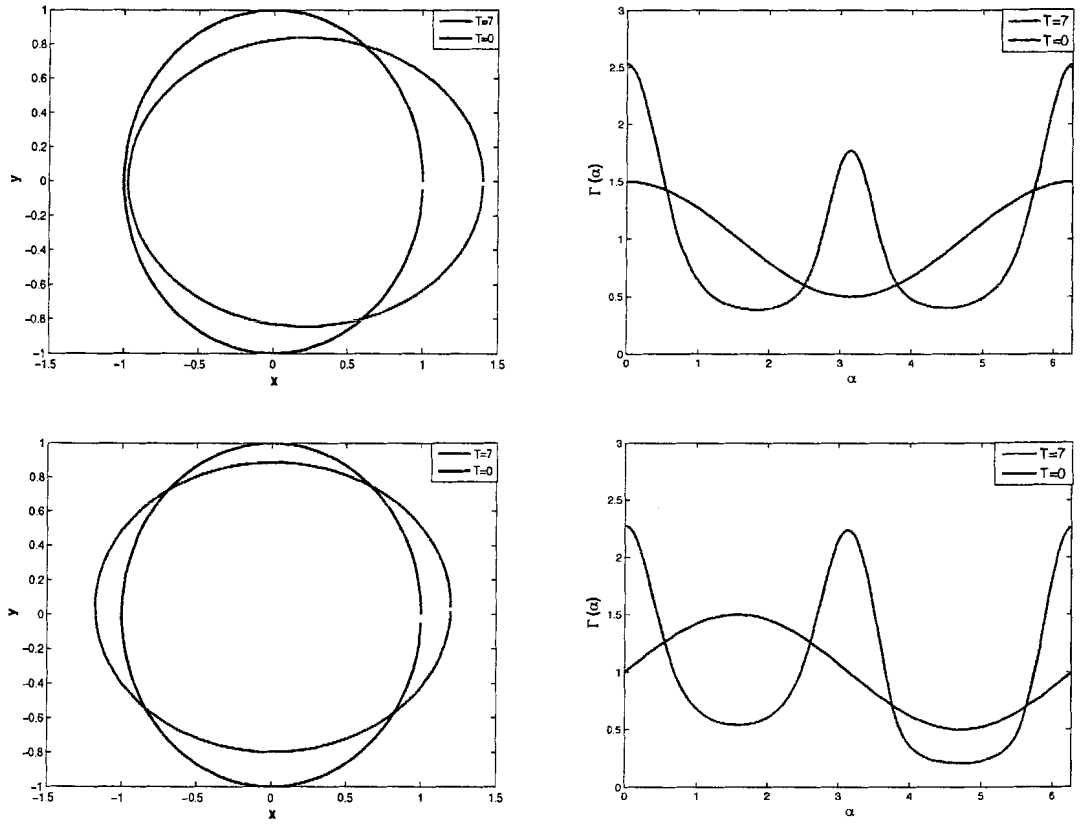

Figure 6.5: *Effects of non-uniform initial surfactant profiles on initially circular bubbles. The top plots show the bubble profile and the surfactant profile for an initially circular bubble with* $\Gamma(\alpha, 0) = 1 + \cos(\alpha)/2$. *The bottom plots show the bubble profile and the surfactant profile for an initially circular bubble with* $\Gamma(\alpha, 0) = 1 + \sin(\alpha)/2$.

Chapter 7

Conclusion and Future Work

In this project, we present a new numerical method to calculate the motion of a bubble interface in a strain Stokes Flow with non-uniform surface tension. This consists of evolving the surfactant equation alongside the interface motion equations. The surfactant dynamics is incorporated into a formulation that uses equal-arclength spacing of the interface marker points to maintain a low-order stability constraint. We exploit the complex variable theory of the biharmonic equation to derive the equations for the problem, as well as recent advances in fast numerical algorithms for the computations.

Our numerical method has five major advantages to previous approaches on this problem. First, it has spectral accuracy. The interface and surfactant are described on a spectral mesh and pseudospectral calculations are used throughout, for example when solving for the velocity at the marker points from the integral equations. Second, the solution of the integral equations is achieved in $\mathcal{O}(N)$ steps using a fast iterative method, where N is the number of marker points. This approach is a necessity for deformed interface or surfactant profiles, where a rather large N is needed to properly resolve the variables. Moreover, this makes the method a fast and efficient tool worthy to consider for large-scale, long-time simulations. Third, by exploiting an Implicit-Explicit scheme for the time-integration of the numerically stiff surfactant equation, we ease the stability constraint on the time-step to linear with respect to the mesh spacing. Fourth, by maintaining an equal arclength spacing of the marker points on the interface, we reinforce the low-order stability constraint. Last, by computing the velocity at double the number of marker points, we ensure the calculations are not prone to high wave-number instabilities that would otherwise arise. We discuss some of these advantages in the context of a few evolving surfactant-laden bubble examples.

7.1 Future Work

In this thesis, we mainly focused in deriving the equations, investigating the numerical algorithm and its stability, and validating the model by comparing it to known test cases or simple scenarios considered in previous works in the area. We were however underpinning the model for future uses of the algorithm. The numerical method we developed is best suited for general bubble shapes and large-scale, long-time simulations of multiple bubble interfaces under surfactant influence. This is the main goal of our next investigation.

An immediate future study following this project is investigating globules where the density of the fluid enclosed by the interface is higher than the density of the surrounding ambient fluid. These are known as drops, and investigating them entails solving the Stokes equations inside the drop as well as outside it. This modification can be done easily and without disrupting the model presented here much. The analysis done in the bubble case can easily carry over. The same can be said for the multiple drop interfaces case.

Future work includes researching the outcomes of using non-linear equations of state in the model, e.g. a logarithmic dependence as seen in the work of Siegel [21]. These other types of surface tension-surfactant dependency relations can give particular insights into various cases of terminal bubble/drop shapes. For example, the logarithmic dependence was used in [21] to study cusped bubbles. This is a case where the linear equation of state we considered in this project breaks down, since in the simulations the surface tension risks becoming negative, a non-physical numerical artifact of the problem.

Another problem of interest is investigating the behavior of shrinking/expanding bubbles/drops in quiescent flows. Our numerical model can be easily modified to account for the change in bubble/drop area. The analytical solutions for polynomial bubbles in the surfactant-laden flows [20, 9] and the numerical studies in the clean flow case [13] can be used as benchmarks to ascertain the results in simple scenarios. Our model can go further in looking at general shapes and multiple interfaces of such bubbles/drops.

Similarly, the model can be adjusted to consider the case of soluble surfactant, i.e. when there is a surfactant flux to/from the surrounding fluid. This is a more realistic physical model for the interfaces in extensional flows, and can lead to interesting insights into the various phenomena observed experimentally, e.g. tip streaming. Our model can be adjusted for this, but a more rigorous analysis needs to be performed to guarantee high accuracy in capturing the surfactant flux. This is future research.

Bibliography

[1] M. Abramowitz and I. A. Stegun, *Handbook of mathematical functions, with formulas, graphs, and mathematical tables* 9th printing, (Dover, New York, 1972)

[2] L. K. Antanovskii, A plane inviscid incompressible bubble placed within a creeping viscous flow: formation of a cusped bubble, *Eur. J. Mech. B/Fluids* **13**, 491 (1994).

[3] U. M. Ascher, S. J. Ruuth and B. M. Wetton: Implicit-explicit methods for time-dependent PDE's. *SIAM J. Numer. Anal.*, **32** 797(1995).

[4] U. M. Ascher, S. J. Ruuth and R. J. Spiteri: Implicit-explicit Runge-Kutta methods for time-dependent partial differential equations. *App. Num. Math.*, **25** 151(1997).

[5] G. Baker and A. Nachbin, Stable methods for vortex sheet motion in the presence of surface tension, *SIAM J. Sci. Comp.* **19**, 1737 (1998).

[6] J. D. Buckmaster and J. E. Flaherty, The bursting of two-dimensional drops in slow viscous flow, *J. Fluid Mech.* **60**, 625 (1973).

[7] J. Carrier, L. Greengard, and V. Rokhlin, A fast adaptive multipole algorithm for particle simulations, *SIAM J. Sci. Statist. Comput.* **9**, 669 (1988).

[8] R. A. De Bruijn, Tipstreaming of drops in simple shear flows, *Chem. Eng. Sci.* **48**, 277 (1993).

[9] J. R. P Gilmore, The calculation of interface motion of a surfactant-laden bubble in Stokes Flow, *M.Sc. Thesis*, (Simon Fraser University 2003).

[10] L. Greengard, M. C. Kropinski, and A. Mayo, Integral equation methods for Stokes Flow and Isotropic Elasticity in the plane, *J. Comp. Phys.* **125**, 403 (1996).

[11] T. Y. Hou, J. S. Lowengrub, and M. J. Shelley, Removing the stiffness from interfacial flows with surface tension, *J. Comp. Phys.* **114**, 312 (1994).

[12] R. A. Johnson and A. Borhan, Stability of the shape of a surfactant-laden drop translating at low Reynolds number, *Phys. Fluids* **12**, No. 4, 773 (2000).

[13] M. C. A. Kropinski, An efficient numerical method for studying interfacial motion in two-dimensional creeping flows, *J. Comp. Phys.* **171**, 479 (2001).

[14] M. C. A. Kropinski, Numerical method for multiple inviscid interfaces in creeping flows, *J. Comp. Phys.* **180**, 1 (2002).

[15] W. E. Langlois, *Slow viscous flow* (Macmillan Co., New York, 1964).

[16] W. J. Milliken, and L. G. Leal, The influence of surfactant on the deformation and breakup of viscous drops. *J. Colloid Interface Sci.* **166**, 275 (1994)

[17] S. G. Muskhelishveli, *Some basic problems of the mathematical theory of elasticity* (Noordhoff, Groningen, 1953).

[18] C. Pozrikidis, Numerical studies of cusp formation at fluid interfaces in Stokes Flow, *J. Fluid Mech.* **357**, 29 (1998).

[19] F. D. Rumsheidt and S. G. Mason, Particle motions in sheared suspensions XII: Deformation and burst of liquid drops in shear flow, *J. Coll. Int. Sci.* **16**, 238 (1961).

[20] M. Siegel, Influence of surfactant on rounded and pointed bubbles in two-dimensional Stokes Flow, *SIAM J. Appl. Math.* **59**, No. 6, (1999).

[21] M. Siegel, Cusp formation for time-evolving bubbles in two-dimensional Stokes flow, *J. Fluid Mech.* **412**, 227 (2000).

[22] S. Tanveer and G. L. Vasconcelos, Time-evolving bubbles in two-dimensional Stokes flow, *J. Fluid Mech.* **301**, 325 (1995).

[23] G. I. Taylor, The formation of emulsions in definable fields of flow, *Proc. R. Soc. Lond. A* **146**, 501, (1934).

[24] H. Wong, D. Rumschitzki, and C. Maldarelli, On the surfactant mass balance at a deforming fluid interface, *Phys. Fluids A* **8**, 3203 (1996).